ELSEVIER

Chemical Geology 231 (2006) 252–284

CHEMICAL GEOLOGY
INCLUDING
ISOTOPE GEOSCIENCE

www.elsevier.com/locate/chemgeo

Fluid sources for the La Guitarra epithermal deposit (Temascaltepec district, Mexico): Volatile and helium isotope analyses in fluid inclusions

Antoni Camprubí [a,*], Beverly A. Chomiak [b,c], Ruth E. Villanueva-Estrada [d], Àngels Canals [e], David I. Norman [b], Esteve Cardellach [f], Martin Stute [g]

[a] *Centro de Geociencias, Universidad Nacional Autónoma de México, Campus Juriquilla, Carretera Querétaro-San Luís Potosí km 15.5, Apartado Postal 1-742, 76230 Santiago de Querétaro, Qro., Mexico*

[b] *Department of Earth and Environmental Science, New Mexico Institute of Mining and Technology, Socorro, New Mexico 87801, USA*

[c] *Department of Physics, Astronomy, and Geophysics, Connecticut College, 270 Mohegan Avenue, New London, Connecticut 06320-4196, USA*

[d] *Posgrado en Ciencias de la Tierra, Universidad Nacional Autónoma de México, Ciudad Universitaria, Delegación Coyoacán, 04510 México, D.F., Mexico*

[e] *Departament de Cristal·lografia, Mineralogia i Dipòsits Minerals, Facultat de Geologia, Universitat de Barcelona, Carrer de Martí i Franquès s/n, 08028 Barcelona, Spain*

[f] *Departament de Geologia, Facultat de Ciències, Universitat Autònoma de Barcelona, 08193 Bellaterra, Spain*

[g] *Lamont-Doherty Earth Observatory, Columbia University, 61 Rte. 9W, 45 Geochemistry Building, Palisades, New York 10964, USA*

Received 11 January 2005; received in revised form 20 December 2005; accepted 1 February 2006

Abstract

The La Guitarra deposit (Temascaltepec district, South-Central Mexico), belongs to the low/intermediate sulfidation epithermal type, has a polymetallic character although it is currently being mined for Ag and Au. The mineralization shows a polyphasic character and formed through several stages and sub-stages (named I, IIA, IIB, IIC, IID, and III). The previous structural, mineralogical, fluid inclusion and stable isotope studies were used to constrain the selection of samples for volatile and helium isotope analyses portrayed in this study. The N_2/Ar overall range obtained from analytical runs on fluid inclusion volatiles, by means of Quadrupole Mass Spectrometry (QMS), is 0 to 2526, and it ranges 0 to 2526 for stage I, 0 to 1264 for stage IIA, 0 to 1369 for stage IIB, 11 to 2401 for stage IIC, 19 to 324 for stage IID, and 0 to 2526 for stage III. These values, combined with the CO_2/CH_4 ratios, and N_2–He–Ar and N_2–CH_4–Ar relationships, suggest the occurrence of fluids from magmatic, crustal, and shallow meteoric sources in the forming epithermal vein deposit. The helium isotope analyses, obtained by means of Noble Gas Mass Spectrometry, display *R*/Ra average values between 0.5 and 2, pointing to the occurrence of mantle-derived helium that was relatively diluted or "contaminated" by crustal helium. These volatile analyses, when correlated with the stable isotope data from previous works and He isotope data, show the same distribution of data concerning sources for mineralizing fluids, especially those corresponding to magmatic and crustal sources. Thus, the overall geochemical data from mineralizing fluids are revealed as intrinsically consistent when compared to each other.

The three main sources for mineralizing fluids (magmatic, and both deep and shallow meteoric fluids) are accountable at any scale, from stages of mineralization down to specific mineral associations. The volatile and helium isotope data obtained in this paper suggest that the precious metal-bearing mineral associations formed after hydrothermal pulses of predominantly oxidized

* Corresponding author. Tel.: +52 55 5623 4116x138; fax: +52 55 5623 4104 to 5623 4119x161.
E-mail address: camprubi@geociencias.unam.mx (A. Camprubí).

0009-2541/$ - see front matter
doi:10.1016/j.chemgeo.2006.02.002

magmatic fluids, and thus it is likely that precious metals were carried by fluids with such origin. Minerals from base-metal sulfide associations record both crustal and magmatic sources for mineralizing fluids, thus suggesting that base metals could be derived from deep leaching of crustal rocks. At the La Guitarra epithermal deposit there is no evidence for an evolution of mineralizing fluids towards any dominant source. Rather than that, volatile analyses in fluid inclusions suggest that this deposit formed as a pulsing hydrothermal system where each pulse or set of pulses accounts for different compositions of mineralizing fluids.

The positive correlation between the relative content of magmatic fluids (high N_2/Ar ratios) and H_2S suggests that the necessary sulfur to carry mostly gold as bisulfide complexes came essentially from magmatic sources. Chlorine necessary to carry silver and base metals was found to be abundant in inclusion fluids and although there is no evidence about its source, it is plausible that it may come from magmatic sources as well.

Keywords: Epithermal; Low/intermediate sulfidation; Fluid inclusions; Gas chemistry; Volatiles; N_2/Ar ratio; He isotopes; Magmatic fluids; Crustal fluids; Meteoric water; La Guitarra; Temascaltepec district; Mexico

1. Introduction: the use of volatile and helium isotope data to trace the sources for mineralizing fluids

Mineralizing fluids involved in the formation of epithermal deposits may be classified by their distinct sources: magmatic fluids, deeply circulated meteoric waters (also named "crustal" waters), sedimentary brines, and shallow meteoric waters (Albinson et al., 2001). Although stable isotope geochemistry is the most used technique to study the contribution of each fluid type in a mineral deposit, the combined analyses of volatiles and helium isotopic ratios in inclusion fluids is a powerful tool to further characterize the origin of fluids in a hydrothermal system or deposit (Hedenquist and Aoki, 1991; Norman and Musgrave, 1994; Albinson et al., 2001; Moore et al., 2001).

The magmatic fluids involved in hydrothermal mineral deposits can be characterized as rhyolite- or mid-ocean ridge basalt-derived. All these fluid types and their mixtures occupy characteristic "regions" in N_2–He–Ar ternary plots (Norman and Musgrave, 1994; Moore et al., 2001). Meteoric waters have N_2–He–Ar compositions between that of air-saturated and crustal waters, and meteoric waters that acquired volatiles from a cooling intrusive body have N_2–He–Ar compositions between those of air-saturated waters and magmatic fluids. As noble gases and N_2 are chemically inert, even when there are inputs or outputs of hydrothermal fluids, a conservative record of their ratios is preserved by the fluids (Ballantine et al., 2002), unless boiling occurs and no vapor-rich fluid inclusions are trapped.

The relative concentrations of N_2–Ar–He in gas samples from active volcanoes associated with hot spots, ocean ridges and convergent plate margins define two different mixing trends between basaltic and andesitic fluids with meteoric waters (Giggenbach, 1992b). The andesitic and basaltic fluids are characterized, respectively, by N_2/He values between 1700 and 5000, and between 10 and 220 (Simmons, 1995). The He/Ar values of these gases are close to the "mantle" value ≈ 3. The air-saturated meteoric waters, with N_2/Ar values between 36 and 50 reflecting the atmospheric influence (N_2/Ar = 84), are usually the end-member of both andesitic and basaltic fluids. The recharge fluids of an active hydrothermal system may have variable amounts of air, and boiling processes can also modify the original N_2/Ar values of hydrothermal fluids. As none of the considered gases (N_2, He, Ar) is reactive in geothermal fluids, their relative concentrations may be useful to complete the He isotope compositions as tracers of the occurrence of deep fluids of magmatic origin (Giggenbach, 1992b; Norman and Musgrave, 1994; Moore et al., 2001), and their analysis can display a clearer approach to the sources of fluids. The data of volatiles from felsic volcanoes (Giggenbach, 1992a), magmatic glass inclusions (Norman et al., 1997a), and fluid inclusions in porphyry copper deposits (Norman and Musgrave, 1994), indicate that magmatic volatiles are characterized by N_2/Ar ratios higher than air. Moreover, the positive correlation between the N_2/Ar ratios and O and H stable isotopes revealing a magmatic source for hydrothermal fluids indicates a magmatic origin for N_2 (Hedenquist and Aoki, 1991).

In epithermal deposits, like Fresnillo in Mexico (Benton, 1991; Norman and Musgrave, 1994; Simmons, 1995), the compositions of gases contained in fluid inclusions are mostly found in the field limited by meteoric and magmatic end-members in the N_2–He–Ar ternary plot. The systematic study of the volatiles contained in fluid inclusions from several Mexican low and intermediate sulfidation epithermal deposits (Norman et al., 1997b; Albinson et al., 2001) suggests that (1) the occurrence of magmatic fluids is manifested in most of them, (2) the contribution of magmatic fluids seems to be more important during the formation of ore-

bearing than barren associations, and (3) the sulfur contribution as H_2S by magmatic fluids is a key factor for the transport of gold and the occurrence of metallic mineralizations. However, support from more conventional techniques, such as O and H stable isotope studies, is still fundamental to trace water to rock interactions and to determine fluid sources or processes associated with the upwelling of hydrothermal fluids. For instance, in N_2–He–Ar or N_2–CH_4–Ar ternary plots, the regions where metamorphic waters occur are still to be determined (Norman and Musgrave, 1994).

The differences between the helium isotope compositions in the atmosphere, the upper mantle, the continental crust, and radiogenic sources, allow their use as tracers of the sources for volcanic and geothermal volatiles (Giggenbach and Poreda, 1993; Giggenbach et al., 1994; Moore et al., 2001). The volatiles in geothermal fields from the Circum-Pacific Rim have *R*/Ra values between 4.3 and 8.2, pointing to the occurrence of important contributions of mantle-derived helium (Torgersen et al., 1982; Poreda and Craig, 1989; Giggenbach and Poreda, 1993; Giggenbach et al., 1994; Patterson et al., 1997, among many others). These values are very similar to those found in phenocrystals and xenoliths from lavas of volcanic arcs, where *R*/Ra range between <1 and 8.5 (Tolstikhin et al., 1974; Hilton and Craig, 1989; Poreda and Craig, 1989; Hilton et al., 1993; Patterson et al., 1994, 1997). In the epithermal deposits of Fresnillo in Mexico and Antamok-Acupan in the Philippines were obtained *R*/Ra values of 1 to 2 and 6 to 7, respectively (Simmons et al., 1988; Cooke and Bloom, 1990). These data display the occurrence of mantle-derived helium that was "diluted" by crustal helium, and were interpreted in the sense that helium was probably transported to the crust by upwelling magmas, and migrated to the upper crust within the hydrothermal mineralizing fluids.

The relationship between magmatic fluids and base and precious metal mineralization during the formation of the La Guitarra deposit was already suggested by Camprubí et al. (2001b) from fluid inclusion, stable and radiogenic isotope data. The vein formation was the result of complex processes during which fluids of several origins were involved, and some ambiguous stable isotope data did not allow to clearly recognize the origin and evolution of fluids involved in each stage of vein formation.

The aim of the present study is twofold: (1) to obtain complementary data in order to characterize the mineralizing fluid sources for the La Guitarra Ag–Au epithermal deposit through the analysis of volatiles and He isotopes trapped in fluid inclusions, and (2) to determine the role of fluid origin in the transport and deposition of base and precious metals in the vein system.

2. The La Guitarra epithermal deposit: previous work

The Temascaltepec district is located 150 km SW of Mexico City, in México state, and is formed by several sets of Ag–Au bearing epithermal veins. Although these deposits were formerly assigned to a low sulfidation type (Albinson et al., 2001; Camprubí et al., 2001a,b), recent reclassification of epithermal deposits by Einaudi et al. (2003) and Sillitoe and Hedenquist (2003) suggests the Temascaltepec district vein deposits have characteristics of both low and intermediate sulfidation types. For this distinction, the reader is encouraged to compare the $T/f(S_2)$ diagrams in Einaudi et al. (2003) and Camprubí et al. (2001a).

In the Temascaltepec area, three main vein sets occur from NW to SE: El Coloso, La Guitarra, and Mina de Agua (Fig. 1) which, based on geological evidence, are assumed to have formed from a single major epithermal vein set (Camprubí et al., 2001a). The outcropping strike length of the vein deposit formed by La Guitarra and El Coloso veins zones altogether is more than 3.5 km, with an observable vertical extent of about 500 m. The maximum vein thickness is about 15 to 20 m, averaging 5 m. The results from previous studies are summarized in Table 1.

2.1. Geology

The veins were mineralized during hydrothermal activity associated with the Tertiary volcanism of the Sierra Madre del Sur (SMS). Host rocks (Fig. 1) comprise the pre-Albian Taxco Schists of the Tierra Caliente metamorphic complex, an early Eocene molasse of the Balsas formation, a middle Eocene biotitic quartz-monzonite stock, and an upper Eocene to Oligocene rhyolitic and andesitic tuff unit of the SMS. The latter includes the rhyolitic feeder neck of Cerro El Peñón, dated at 34.87±0.15 Ma by the $^{40}Ar/^{39}Ar$ method (Blatter et al., 2001). The La Guitarra deposit is hosted by the late-Laramide granitic suite, whilst the veins of El Coloso area are hosted by all the lithological units mentioned above. These units are covered by basalt and andesite flows of the Trans-Mexican Volcanic Belt (TMVB), which range in age from late Miocene to the present. The epithermal veins were dated at 32.9±0.1 and 33.3±0.1 Ma by the $^{40}Ar/^{39}Ar$ method on adularia samples (Camprubí et al., 2003).

2.2. Mineralogy

The hydrothermal alteration around the veins in the La Guitarra deposit and neighboring areas is weakly developed. Propylitic alteration forms the outermost zone, becoming quartz-sericitic in the vicinity of quartz-filled veins and veinlets, and kaolinite–illite–smectite alteration dominates the upper part of the deposit. Quartz-sericite haloes developed around the veins, but the intensity of the alteration is strong only in the vicinity of the vein contact.

The vein stratigraphy of the La Guitarra deposit can be grouped in three mineralization stages. Stage I is dominated by a base-metal sulfide association whereas stages II and III contain most of the precious-metal assemblages. Mineral relative abundance in each mineralization stage reflects the increase on the content of Ag–Au minerals with time. Thus stage III is the richest in precious metals of the three stages, with base metals of stage I lacking in Au. Stage II is the most important in volume and contains the main mineralization (sub-stage IIB). Base-metal sulfides precipitated early in all mineralization stages, and their relative content increases with depth at any stage. Furthermore, Ag–Au minerals occur later within each assemblage and their relative amount increases towards the upper parts of the deposit. Only in stage III the content of precious-metal minerals increases with depth, compared to base-metal minerals. Crystals, pseudomorphs and phantoms of bladed calcite and pseudorhombohedral adularia crystals are evidence of boiling, and are widespread in stages IIA and IIB. Whereas in stage I quartz pseudomorphs after bladed calcite are associated with silver mineral assemblages, these occurrences are very restricted in space (Camprubí et al., 2001a).

2.3. Fluid inclusion and stable isotope data

Temperature and salinity values of mineralizing fluids span ranges of 80 to 266 °C and 0.8 to 14.4 wt.% NaCl equiv, respectively (Camprubí et al., 2001b). Paragenetic constraints demonstrate that the temperature and salinity of the solutions decreased with time. Base-metal sulfides deposited from solutions of 6 to 14 wt.% NaCl equiv whereas precious-metal mineralization and quartz deposited from solutions of 1 to 10 wt.% NaCl equiv. To account for the relatively high salinities found

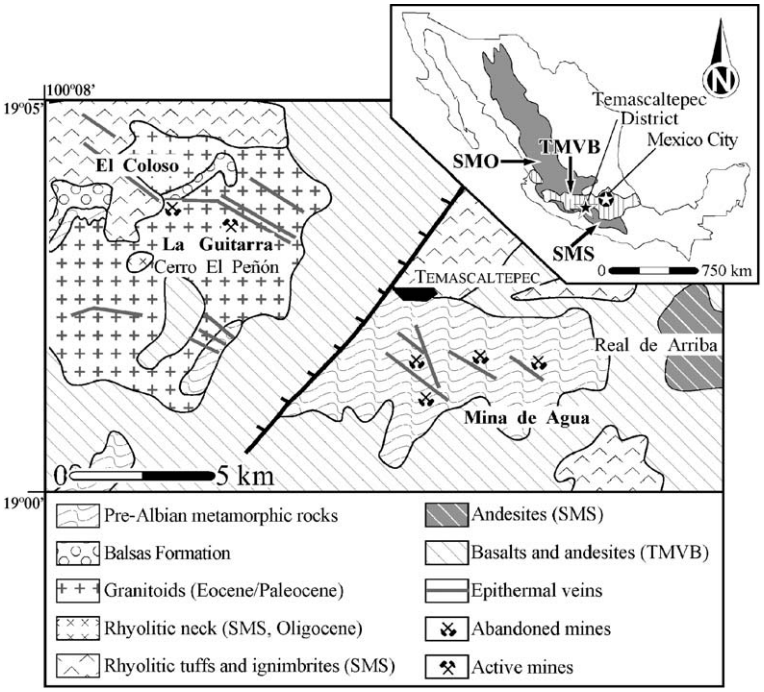

Fig. 1. Geological map of the Temascaltepec district. See data sources in Camprubí et al. (2001a). The outlined area with Tertiary to present volcanism is simplified from Ferrari et al. (2002), and Morán-Zenteno et al. (1999) for the volcanism south of the Trans-Mexican Volcanic Belt. Key: SMO = Sierra Madre Occidental; SMS = Sierra Madre del Sur; TMVB = Trans-Mexican Volcanic Belt.

Table 1
Summary of mineralogical and physicochemical data from the La Guitarra epithermal deposit, Temascaltepec district (Camprubí et al., 2001a,b, and this work)

	Stage I	Stage IIA	Stage IIB	Stage IIC	Stage IID	Stage III
Structure and composition						
	Breccias cemented by banded quartz with dominant base-metal sulfides; low Ag content and no Au	Banded and brecciated quartz; contains no metallic mineralization	Banded and brecciated quartz; contains the main mineralization, either in pre- and post-brecciation bands	Banded and massive quartz; contains no metallic mineralization	Veinlet arrays forming stockworks and crackle breccias: contains no Ag–Au mineralization	Veinlets seldom coalescing into stockwork lenses; contains the highest concentration of Ag–Au minerals
Mineralogy						
Association 1	Quartz, pyrite, sphalerite, galena, fluorite, siderite, ankerite, chalcopyrite, illite to smectite clays, kaolinite *(base-metal sulfide association)*	Quartz, chalcedony, opal, bladed calcite phantoms, adularia	Quartz, chalcedony, bladed calcite phantoms, adularia, sericite, pyrite, sphalerite, galena	Quartz, chalcedony, opal	Quartz, pyrite, sphalerite, galena, marcasite, stibnite *[or]* quartz, sphalerite, galena, pyrite, greenockite	Quartz, pyrite, sphalerite, galena, marcasite, chalcopyrite
Association 2	Quartz, veenite, twinnite		Ag-tetrahedrite–tennantite, proustite–pyrargyrite, pearceite–polybasite, miargyrite, argentite, electrum, chalcopyrite, xanthoconite–pyrostilpnite, stephanite–arsenostephanite, marcasite, Sb-billingsleyite, barite			Ag-tetrahedrite–tennantite, electrum
Association 3	Quartz, bladed calcite, argentite, Sb-billingsleyite, proustite–pyrargyrite, xanthoconitepyrostilpnite, freieslebenite, andorite, miargyrite *(silver-mineral association)*		Enargite, siderite, ankerite, kutnahorite			Galena, diaphorite, miargyrite, pearceitepolybasite, proustitepyrargyrite, xanthoconite–pyrostilpnite, ramdohrite, sternbergite, chalcopyrite, siderite, calcite, ankerite

FeS content in sp *(mole fraction)*	0.01 (association 1) 0.01–0.25 (association 3)	–	Up to 0.17	–	0.01	0.01
Evidence of boiling?	Yes	Yes	Yes	No	No	No
Fluid inclusions *(in parentheses, number of fluid inclusions where Th and TmI were measured, respectively)*						
Minerals	sp, qz, fl	qz	qz	qz	qz	pr–pg
Th (°C)	102 to 273 *(447)*	80 to 256 *(391)*	103 to 228 *(249)*	98 to 208 *(86)*	118 to 197 *(22)*	Some day...
Tm_I *(°C)*	−1.2 to −10.4 *(601)*	−0.6 to −6.1 *(499)*	−1.5 to −3.9 *(295)*	−0.5 to −3.3 *(105)*	−1.6 to −3.5 *(27)*	Some day...
Wt.% NaCl eq	2.0 to 14.4	1.1 to 9.3	2.6 to 6.2	0.8 to 5.3	2.6 to 5.6	–
Mineral geothermometers *(in parentheses, number of samples where mineral assemblages suitable for geothermometry were found)*						
Assemblage	ag, mi, pg, pr, ps, xt	–	ag, bl, mi, pg, pr, ps, st, xt	–	–	ag, mi, pg, pr, ps, xt
T range (°C)	≥170 to 197 *(5)*	–	≥120 to 197 *(7)*	–	–	≥180 to ≥240 *(5)*
Stable isotopes *(in parentheses, number of samples analyzed)*						
$\delta^{18}O_{quartz}$ *(‰)*	14.8 to 19.0 *(8)*	15.6 to 19.2 *(8)*	10.6 to 18.7 *(15)*	17.1 *(1)*	15.6 *(1)*	19.1 *(1)*
$\delta^{18}O_{water}$ *(‰)*	1.8 to 5.8	0.7 to 6.4	−1.5 to 6.9	3.2	2.1	7.3
δD_{water} *(‰)*	−32 *(1)*	−60 to −28 *(3)*	−49 to −20 *(3)*	−23 *(1)*	−103 *(1)*	–
$\delta^{34}S_{sulfide}$ *(‰)*	−12.7 to −1.9 *(15)*	–	−6.0 *(1)*	–	−36.6 to −1.2 *(6)*	−0.5 *(1)*
QMS analyses *(in parentheses, number of samples analyzed plus total number of analyses)*						
Minerals	sp, qz, fl	qz	qz, and mixed qz and sulfides	qz	qz	Mixed qz and sulfosalts
N_2/Ar *range*	0 to 2526 *(4 and 42)*	0 to 1264 *(2 and 21)*	0 to 1369 *(5 and 51)*	11 to 2401 *(1 and 10)*	19 to 324 *(1 and 10)*	0 to 2526 *(1 and 15)*

Abbreviations: ag = argentite, bl = Sb-billingsleyite, fl = fluorite, mi = miargyrite, pg = pyrargyrite, pr = proustite, ps = pyrostilpnite, qz = quartz, sp = sphalerite, st = stephanite, xt = xanthoconite.

in La Guitarra, Camprubí et al. (2001b) argued that these were probably related to magmatic exhalations, as no connate brines or evaporites can be inferred from the regional geology.

$\delta^{18}O$, δD and $\delta^{34}S$ values span compositional ranges of $<-1.5‰$ to $>7.3‰$, $-103‰$ to $-20‰$, and $-36.6‰$ to $-0.5‰$, respectively (Camprubí et al., 2001b). The lowest values of δD and $\delta^{34}S$ belong to stage IID, pointing to processes and sources for chemical components that are different from those recorded in the other mineralization stages. Stage IID reveals the occurrence of meteoric fluids that have undergone extensive water–rock interaction and possibly bacteriogenic reduction of dissolved sulfate to H_2S during a lull of the hydrothermal activity in the deposit. The general values from the stages other than IID point to magmatic and meteoric sources for mineralizing fluids. The occurrence of both magmatic and meteoric fluid end-members can be inferred in all stages, but the presence of hydrocarbons in late fluid inclusions of stages IIA and IIB probably indicates some interaction between hydrothermal fluids and sedimentary-metamorphic rocks. $\delta^{34}S$ values of stages other than IID also account for both magmatic and meteoric-sedimentary sources in different proportions. Stage III reveals the strongest influence of magmatic sources for water and sulfur, as it records the highest $\delta^{18}O_{water}$ and $\delta^{34}S$ values of the deposit.

As stated above, evidence was noted for boiling in stages I, IIA and IIB. Although petrographic evidence for boiling in ore bands of stage IIB rarely occur in the same place, the coincident space distribution of these features and the highest Ag and Au grades indicate that metallic mineral deposition during stage IIB was likely induced by boiling. Ore bands of stage IIB generally deposited at higher temperatures than earlier and later barren bands, and $\delta^{18}O$ values are higher in ore bands than in barren bands, possibly indicating a higher magmatic contribution in ore-bearing bands. Mineral precipitation in stages IIC and IID may have occurred by the mixing of upwelling fluids with descending meteoric waters. Mineral precipitation during stage III could either occur by fluid mixing or conductive cooling of hydrothermal fluids. Although hydrothermal flow during stage IID was favored by faulting, the relatively scarce mineralization displayed suggests that the hydrothermal activity was waning. Thus, the key factor that lead to metallic mineral deposition at La Guitarra during any stage of mineralization may more likely have been the occurrence of pulses of magmatic fluids bearing metals in solution, rather than the occurrence of any specific precipitation mechanism at the site of deposition.

3. Sampling and analytical procedure

Volatiles contained in fluid inclusions from fourteen representative samples were analyzed. The analyzed samples were selected from the different stages of vein formation and the most representative mineral associations following paragenetic, fluid inclusion, and stable isotope constraints (Camprubí et al., 2001a,b). Four samples are from stage I: two sphalerite and one fluorite sample from the base-metal sulfide association (BMSA), and one quartz sample that grew interstitially to bladed calcite crystals from the silver mineral association (SMA). Two quartz samples were used from stage IIA, both from post-brecciation bands. Five samples are from stage IIB: two from pre-brecciation quartz bands, one from mineralized bands with mixed quartz, sulfides and sulfosalts, and two from quartz vugs of post-brecciation bands. Two quartz samples were also used from the latest precipitates of stages IIC and IID, and one sample from stage III, containing both the early association of Ag-tetrahedrite with base-metal sulfides and electrum, and a late association of Ag and Ag–Pb sulfosalts.

Volatile analyses were done in a Balzers QMS 420 quadrupole mass spectrometer at the Earth and Environmental Science Department of the New Mexico Institute of Mining and Technology (Socorro, NM). All the analyses were performed using the crush-fast-scan (CFS) method described by Norman et al. (1997a) and Moore et al. (2001). Samples were crushed under vacuum, and the volatiles released were extracted with a high-vacuum pump, ionized by low-energy electrons, and immediately measured by the quadrupole mass spectrometer. During the analysis, the vacuum conditions within the spectrometer and the extraction line were about 1×10^{-7} to 4×10^{-7} Torr and 6×10^{-8} to 1×10^{-7} Torr, respectively. The signal counting per analysis was of 100–120 cycles at 10–20 ms/cycle. The results are reported as mole per cent in the Appendix. In this case the thermal decrepitation–cryogenic separation method (TDCS) was not used, although such method provides the greatest precision. See a comparison of the TDCS and CFS extraction and scan methods with their advantages and limitations in Moore et al. (2001). The crushing method releases volatiles from far less inclusions than those released by decrepitation, but each crush-and-scan cycle analyzes different groups of inclusions, although it does not allow to know the petrographic type of the groups of inclusions that are crushed. The main advantages of the CFS method are that it allows to obtain several analyses from small amounts of a sample and it may also

potentially help to explain processes as fluid mixing or boiling using data from a single sample. Then, the TDCS and CFS methods are the quality versus quantity versions of the QMS technique.

Four samples were selected for helium isotope analyses: one sphalerite sample from the base-metal sulfide assemblage of stage I, and three quartz samples from stages I, IIB and IIC. Helium isotopes were measured using the method of Nier and Schlutter (1985), in a VG 5400 noble gas mass spectrometer, at the Lamont–Doherty Earth Observatory of the Columbia University (Palisades, NY). Gas extraction from fluid inclusions was performed by crushing the samples using an electromagnet-driven piston under vacuum. Before and after each analysis a blank and a reference atmospheric standard were measured using the same device. The atmospheric standard analyzed determined the Ra value used as a reference for the *R* values obtained in the samples. The crushing device consists of an electromagnet-driven piston. The integration time of analysis was 1 h, doing five crushing cycles per sample. For each cycle the detector was positioned in the deuterium mass, which is the most similar to that of helium, making the piston work during 30 s, and then

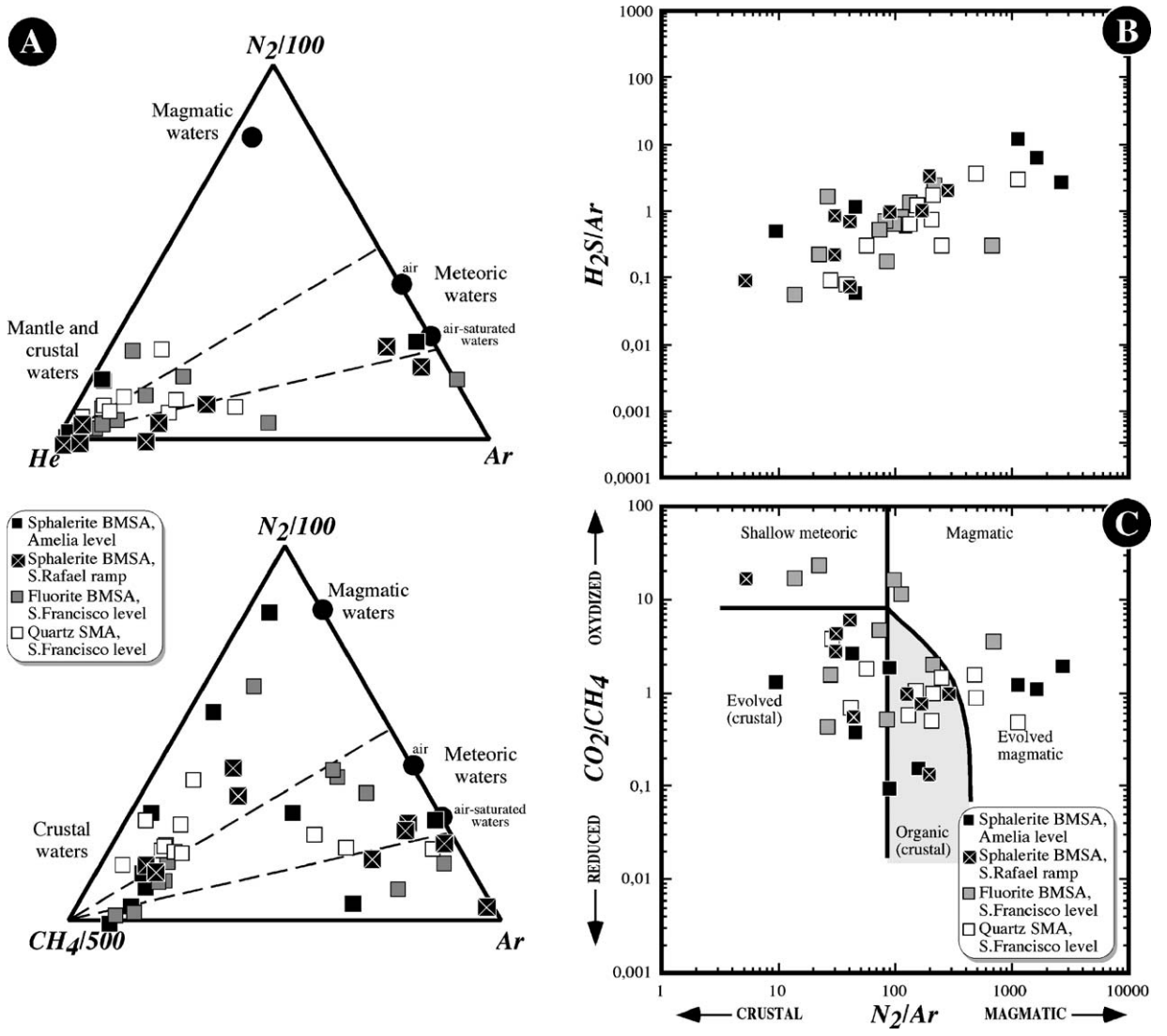

Fig. 2. (A) N_2–He–Ar and N_2–CH_4–Ar ternary plots, (B) correlation diagram between N_2/Ar and H_2S/Ar ratios, and (C) correlation diagram between N_2/Ar and CO_2/CH_4 ratios, after the compositional analyses of volatiles contained in fluid inclusions from stage I. The named levels of underground mining are found at the following elevations above the sea level: San Francisco level at 2250 m, Amelia level at 2175 m, San Rafael ramp at 2070 m (average elevation).

leaving the electromagnet to cool during 10 min. The helium released this way is kept in a helium + carbon trap at ~16 K, that is heated up to 45 K to release the cumulated helium, and then driven towards the mass spectrometer. This process is done ten times during each crushing cycle. The high-precision helium isotope analysis needs a filament current of about 800 μA. The VG 5400 mass spectrometer uses an ion source of electron impact. The electrons emitted by the filament are forced to follow a circular path induced by the source magnets to increase the ionization probability of the gas atoms inside the ionization chamber. Then, the ions are extracted from the ionization chamber, accelerated at 4.5 keV, and differentially deviated by a separation magnet.

4. Results and discussion

4.1. Volatiles (N_2, He, Ar, CH_4, CO_2)

The obtained relative contents of various volatile species are displayed in the Appendix. The N_2–He–Ar,

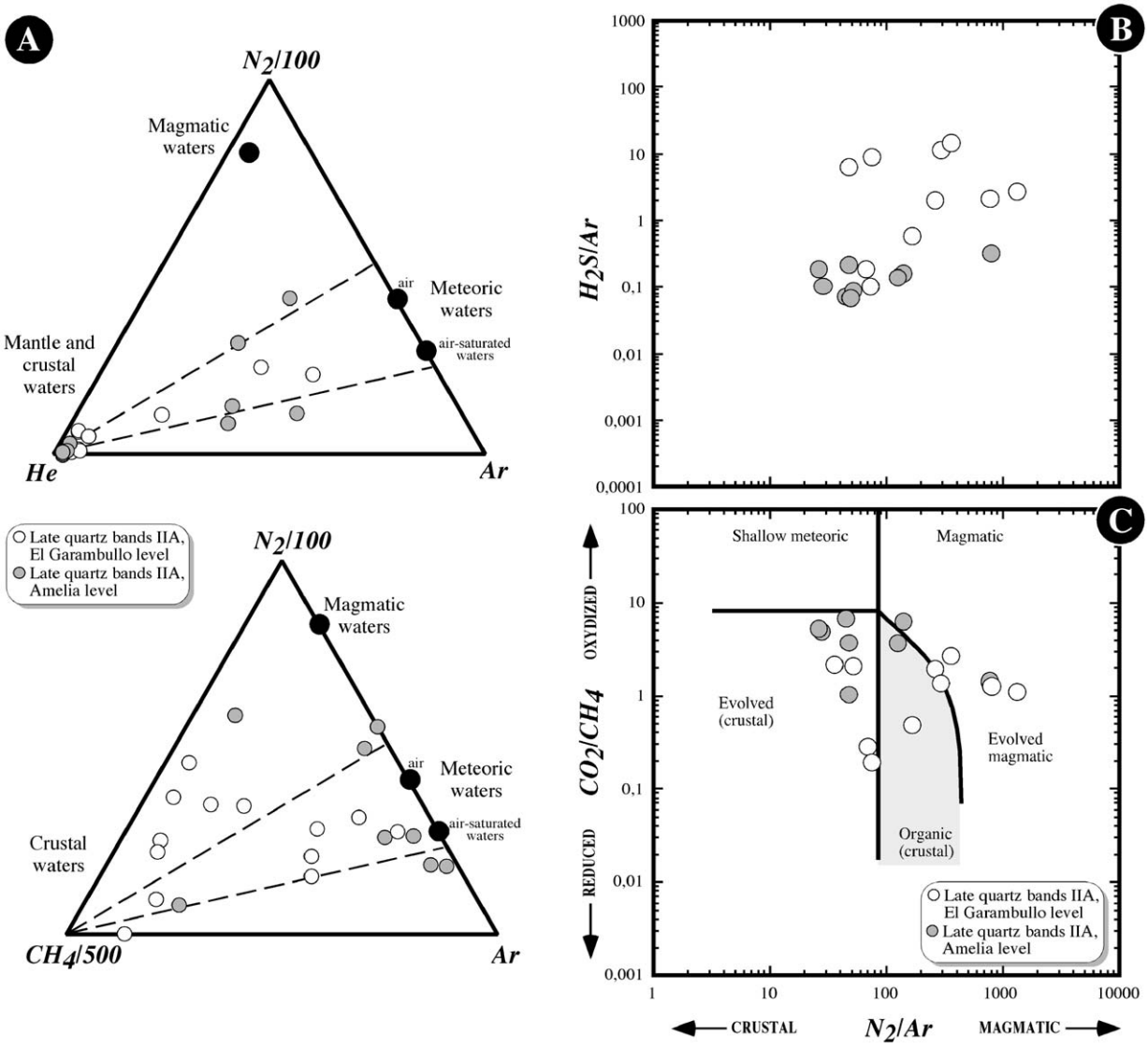

Fig. 3. (A) N_2–He–Ar and N_2–CH_4–Ar ternary plots, (B) correlation diagram between N_2/Ar and H_2S/Ar ratios, and (C) correlation diagram between N_2/Ar and CO_2/CH_4 ratios, after the compositional analyses of volatiles contained in fluid inclusions from stage IIA. The named levels of underground mining are found at the following elevations above the sea level: El Garambullo level at 2425 m, Amelia level at 2175 m.

N_2–CH_4–Ar and N_2/Ar–CO_2/CH_4 plots for samples from stage I (Fig. 2) show a composite origin for mineralizing fluids between magmatic, meteoric and crustal sources. The coincidence between the fluids of rhyolitic origin and deeply circulated meteoric waters in the He apex of the N_2–He–Ar diagram does not allow to discriminate the results that plot in the area between both sources. However, in the N_2–CH_4–Ar diagram, the CH_4 apex is only occupied by deeply circulated meteoric waters and may help to distinguish between the above sources for hydrothermal fluids. The N_2/Ar–CO_2/CH_4 diagram (Fig. 2) shows the relation between oxidized and crustal fluids (shallow meteoric waters), and reduced magmatic fluids. The dispersion of data in that diagram may be due to the occurrence of reduced crustal fluids (deeply circulated meteoric fluids) in the hydrothermal system.

In stage I, results from the base-metal sulfide association (BMSA) and those from the silver mineral association (SMA) can be explained differently. Data

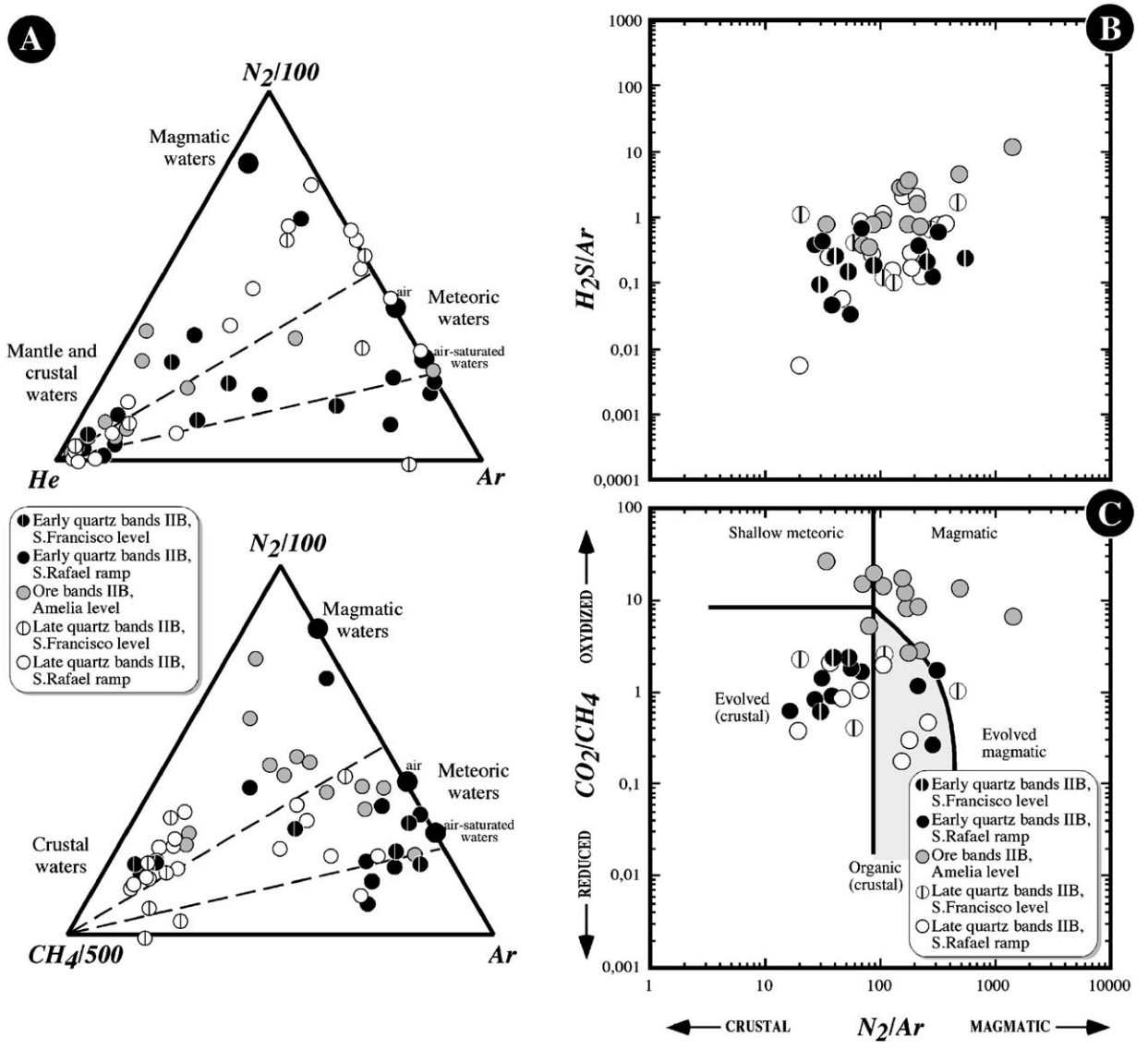

Fig. 4. (A) N_2–He–Ar and N_2–CH_4–Ar ternary plots, (B) correlation diagram between N_2/Ar and H_2S/Ar ratios, and (C) correlation diagram between N_2/Ar and CO_2/CH_4 ratios, after the compositional analyses of volatiles contained in fluid inclusions from stage IIB. The named levels of underground mining are found at the following elevations above the sea level: San Francisco level at 2250 m, Amelia level at 2175 m, San Rafael ramp at 2070 m (average elevation).

from fluorite of the BMSA show a marked influence from meteoric waters, as most of them are found in the compositional field of crustal waters, although some analyses also indicate a magmatic component. On the other side, the data from sphalerite of the BMSA may suggest a stronger influence from magmatic fluids. In the N_2–He–Ar diagram, data from sphalerite mostly plot close to the He apex, thus pointing to a stronger influence of fluids associated with rhyolitic melts and deeply circulated meteoric waters. The data from quartz of the SMA show the occurrence of fluids predominantly from mantle and crustal sources during mineralization, with minor shallow meteoric and magmatic inputs.

Similar to stage I, the N_2–He–Ar diagram for the data from late quartz bands of stage IIA (Fig. 3) shows a dominant component of crustal, deeply circulated meteoric waters, although some data again point to the occurrence of magmatic fluids. Thus, fluids associated with the formation of stage IIA are related to deeply circulated (crustal) and "fresh" meteoric waters, with a minor contribution from magmatic fluids. However, the contribution from magmatic fluids may more clearly be

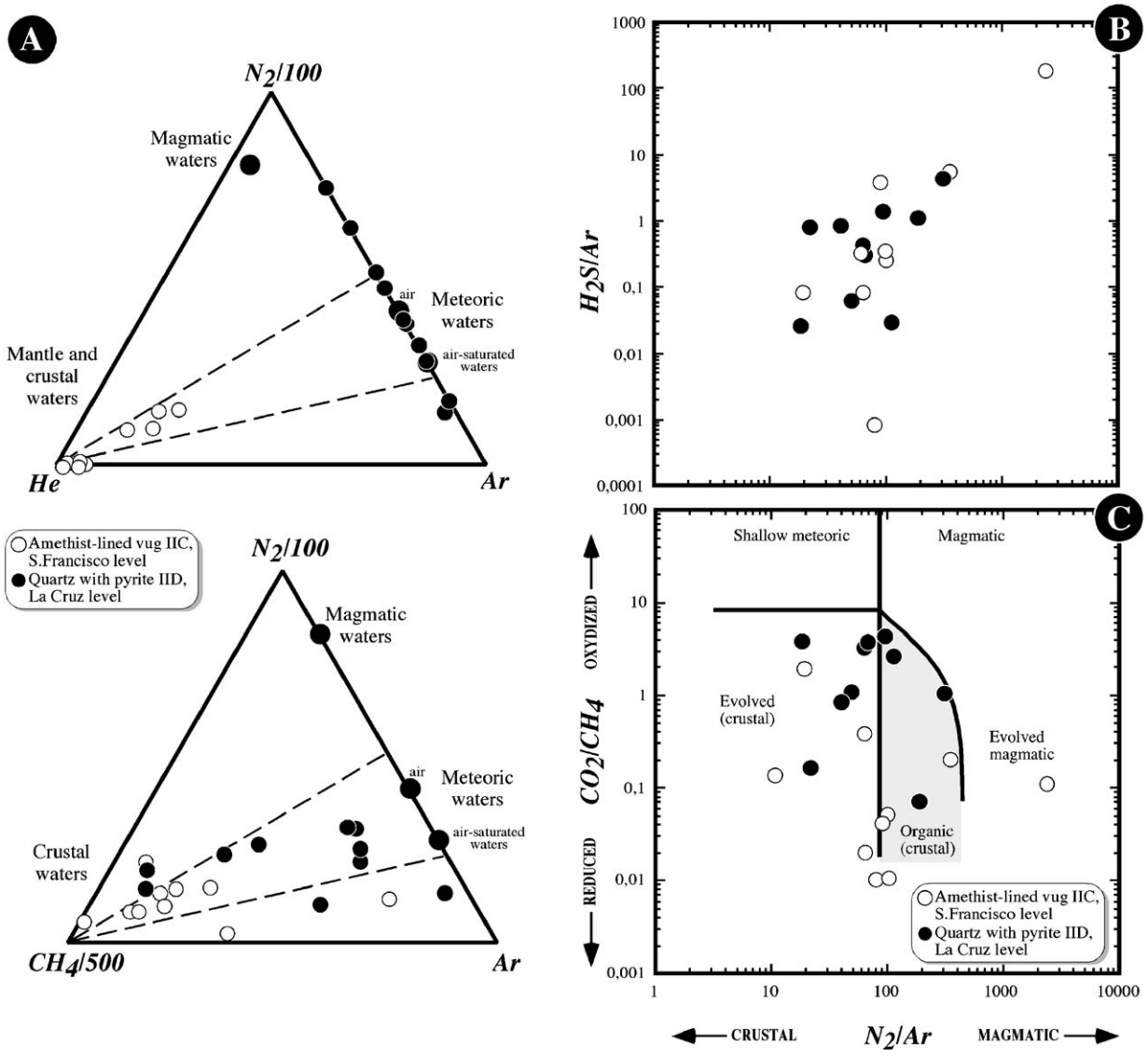

Fig. 5. (A) N_2–He–Ar and N_2–CH_4–Ar ternary plots, (B) correlation diagram between N_2/Ar and H_2S/Ar ratios, and (C) correlation diagram between N_2/Ar and CO_2/CH_4 ratios, after the compositional analyses of volatiles contained in fluid inclusions from stages IIC and IID. The named levels of underground mining are found at the following elevations above the sea level: La Cruz level at 2350 m, San Francisco level at 2250 m.

recognized in N_2–CH_4–Ar and N_2/Ar–CO_2/CH_4 diagrams.

Data from samples of stage IIB in N_2–He–Ar, N_2–CH_4–Ar and N_2/Ar–CO_2/CH_4 diagrams (Fig. 4) suggest the occurrence of fluid of different origin for the different sets of banded mineralization: (a) barren pre-brecciation, (b) ore-bearing, and (c) barren post-brecciation bands. Although all the analyzed samples record the same fluid sources as in stages I and IIA, it is observed that: (1) the fluids associated with barren pre-brecciation bands record the strongest influence of meteoric and crustal waters; (2) ore-bearing bands record the highest magmatic influence, although crustal and meteoric waters are also involved; (3) the fluids associated with barren post-brecciation bands have the same origin manifested by ore-bearing bands, but they record a higher content of crustal, deeply circulated meteoric waters.

N_2–He–Ar, N_2–CH_4–Ar and N_2/Ar–CO_2/CH_4 diagrams for samples from stages IIC and IID (Fig. 5) indicate that these stages were dominated by the occurrence of meteoric waters, with a variable crustal influence. Still, some analyses may reflect that a

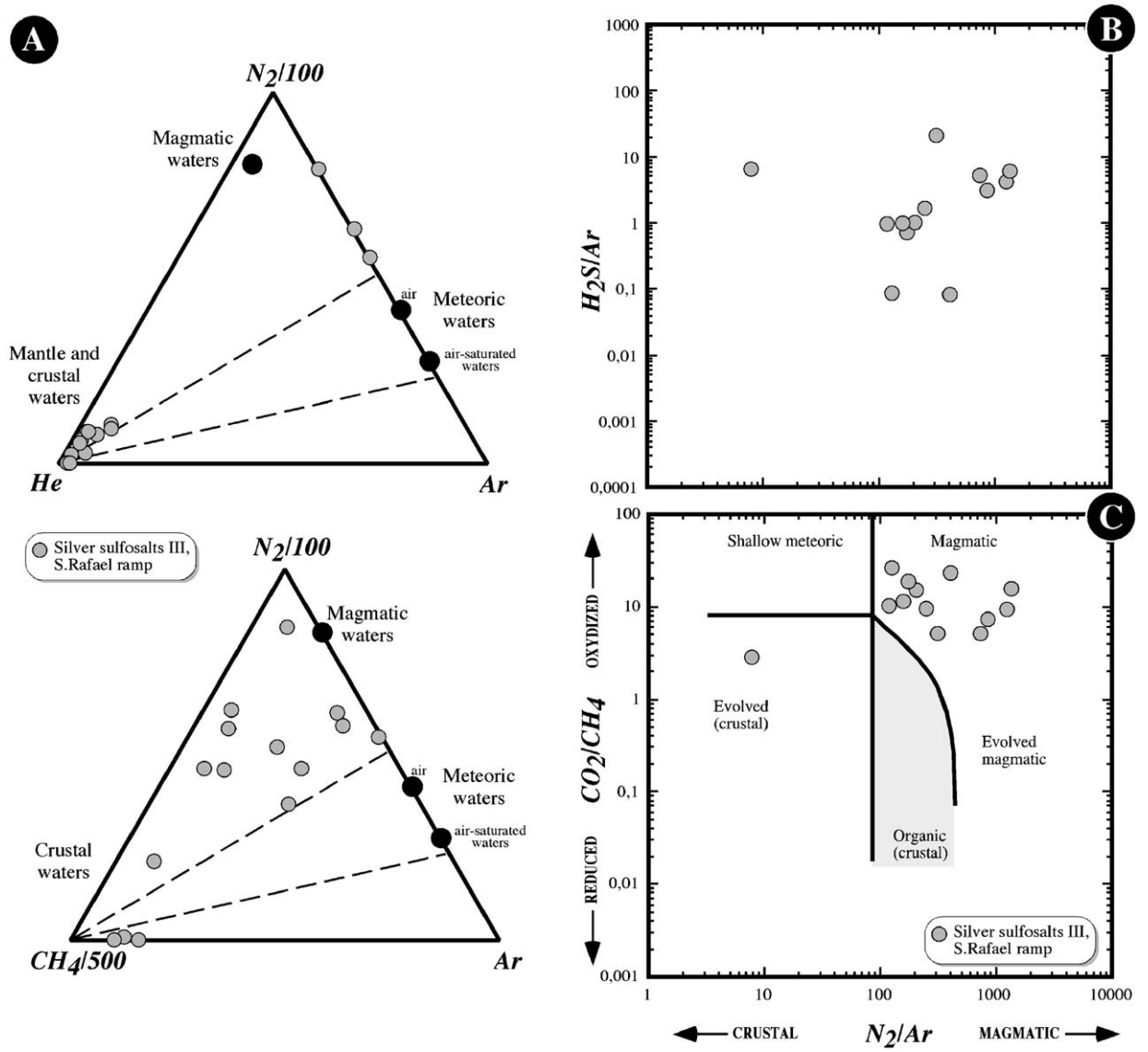

Fig. 6. (A) N_2–He–Ar and N_2–CH_4–Ar ternary plots, (B) correlation diagram between N_2/Ar and H_2S/Ar ratios, and (C) correlation diagram between N_2/Ar and CO_2/CH_4 ratios, after the compositional analyses of volatiles contained in fluid inclusions from stage III. The named levels of underground mining are found at the following elevations above the sea level: San Rafael ramp at 2070 m (average elevation).

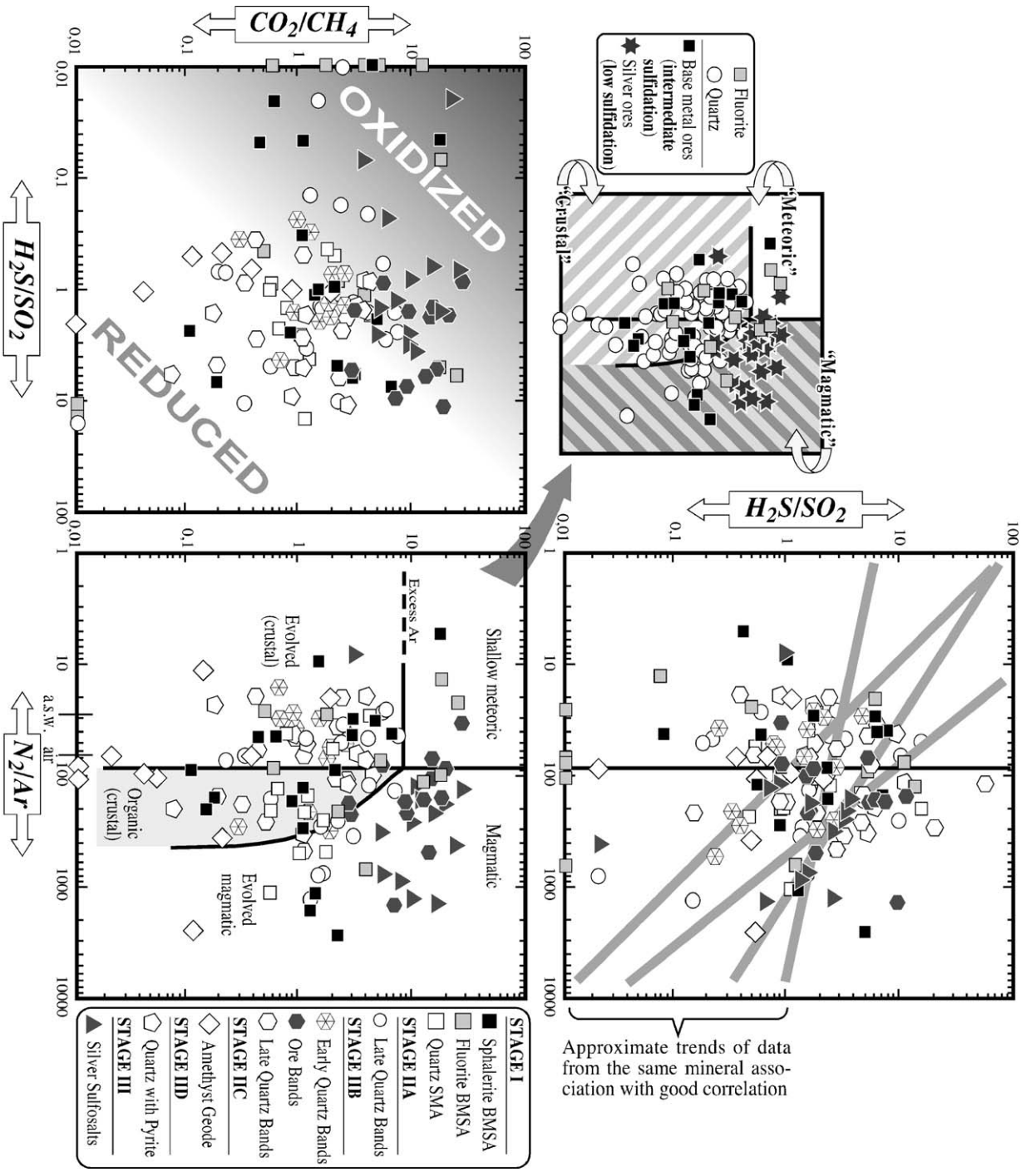
Fluorite
Quartz
Base metal ores (intermediate sulfidation)
Silver ores (low sulfidation)
"Meteoric"
"Magmatic"
"Crustal"
H_2S/SO_2
CO_2/CH_4
OXIDIZED
REDUCED
Approximate trends of data from the same mineral association with good correlation
Shallow meteoric
Magmatic
Excess Ar
Evolved (crustal)
Organic (crustal)
Evolved magmatic
a.s.w.
air
N_2/Ar
STAGE I
Sphalerite BMSA
Fluorite BMSA
Quartz SMA
STAGE IIA
Late Quartz Bands
STAGE IIB
Early Quartz Bands
Ore Bands
Late Quartz Bands
STAGE IIC
Amethyst Geode
STAGE IID
Quartz with Pyrite
STAGE III
Silver Sulfosalts

certain magmatic contribution that, although less significant than in the previous stages, can not be disregarded. The main difference between the fluids associated with stage IIC and those associated with stage IID is that the latter display a greater influence of shallow meteoric waters. In contrast, the N_2–He–Ar, N_2–CH_4–Ar and N_2/Ar–CO_2/CH_4 diagrams for stage III (Fig. 6) exhibit the most clear evidence for the occurrence of magmatic fluids of the whole deposit, although a minor contribution of meteoric waters was also associated with the mineralization.

The positive correlation between N_2/Ar and H_2S/Ar ratios found in most samples (Figs. 2C 3C 4C 5C and 6C) is similar to that reported by Albinson et al. (2001) in the Zacatecas, Maguarichic, Bacís, Zacualpan and El Oro deposits. Hence, in the case of La Guitarra, it is also likely that the H_2S necessary to carry gold as bisulfide complexes came mostly from magmatic sources. The positive correlation between the relative content of H_2S and the N_2/Ar ratio in the fluids supports the hypothesis that H_2S was mainly related to the magmatic component in the mineralizing fluids.

The correlation between H_2S and the N_2/Ar ratio is better observed in gas analyses from sulfides and sulfosalts than in analyses from gangue minerals. The distribution of values from sulfides and sulfosalts has a smaller dispersion, revealing the most outstanding magmatic fluid component. $\delta^{34}S$ data of sulfides and sulfosalts from Camprubí et al. (2001b), as stated above, indicate a mixing between magmatic and sedimentary or metasedimentary sources for sulfur, consistent with volatile analyses.

Stage IIA records the best example of mixing between upwelling hydrothermal fluids and shallow meteoric waters (see Table 1, and Figs. 3 and 7). The higher dispersion of stage IIA data suggests a greater degree of fluid mixing than during stage IIB, where sample AM-9A-3 (see Appendix) presents volatile compositions dominated by shallow oxidized meteoric waters (Figs. 3 and 7). It might be expected that the influx of shallow meteoric waters could be better illustrated by fluids from sample GB96-1 than those from sample AM-9A-3, since the former was obtained at a higher elevation and thus situated in a section of the vein that formed closer to the paleosurface.

Table 2
Helium isotope compositions of fluid inclusions from the La Guitarra deposit

Sample number (weight)	Mineral and stage	$^3He/^4He$	$R/Ra \pm \sigma$
AM-3 (0.449 g)	Sphalerite (BMSA, stage I)	2.78±0.60	2.0±0.4
SF96-12 (1.107 g)	Quartz in bl. cc. (SMA, stage I)	0.74±0.06	0.5±0.1
SF96-3C (0.744 g)	Quartz (late bands, stage IIB)	2.56±0.70	1.8±0.5
SF96-2 (0.735 g)	Quartz (late geode, stage IIC)	1.60±0.18	1.2±0.1

bl.cc. = bladed calcite, BMSA = base-metal sulfide assemblage, SMA = silver mineral assemblage.

4.2. Helium isotopes

The obtained $^3He/^4He$ ratios range between 0.5 and 2 times Ra and are displayed in Table 2. Results are reported as mean values of all the analyses carried out in each sample. These Ra values are consistent with the occurrence of a mantle-derived helium component although, as in the Santo Niño vein of the Fresnillo district (Simmons et al., 1988), this component is relatively "diluted". Although the obtained data present a relatively wide statistic dispersion, a mantle source for helium is still consistent.

A typical mantle-derived $^3He/^4He$ ratio may be modified by several mechanisms. The accumulation of radiogenic ^4He in buoyant magmas is generally associated with a long residence period of the magma in the continental crust (Simmons, 1995). The result is the contamination by crustal-derived helium, whose R/Ra is ~0.1. This hypothesis is considered to be the most plausible in the Fresnillo district, as the continental crust below is relatively thick (Aiken et al., 1988; Gomberg et al., 1988; Nava et al., 1988; Schellhorn et al., 1991; Molina-Garza and Urrutia-Fucugauchi, 1993; Morán-Zenteno et al., 1996). The ^4He can be also added to the hydrothermal fluids as leaching of the crustal rocks proceeds, as a part of the hydrological cycle. Mixing of mantle-derived fluids with meteoric waters is an additional dilution mechanism of a magmatic isotopic composition of helium. In this case, it is remarkable that the $^3He/^4He$ ratio of hydrothermal fluids from geothermal systems decreases from the volcanic centers

Fig. 7. Correlation diagrams between N_2/Ar and H_2S/SO_2, H_2S/SO_2 and CO_2/CH_4, and N_2/Ar and CO_2/CH_4 ratios for the samples analyzed from all stages of mineralization at the La Guitarra deposit (compiled from Figs. 2C 3C 4C 5C and 6C). The positions of the boundaries were taken from Norman and Moore (1999). N_2/Ar ratios lower than 15 indicate loss of N_2 or addition of Ar, labeled as "excess Ar". The terms "early" and "late" are referred to pre- and post-brecciation bands, respectively. In these correlation diagrams N_2/Ar ratios = 0 were skipped, since the absence of N_2 that the corresponding analytical runs recorded do not correspond to an actual lack, but to analytical problems instead; all the analytical runs are reported in the Appendix. Key: a.s.w. = air-saturated water, BMSA = base-metal sulfide association, SMA = silver mineral association.

outwards, due to the increasing water/rock interaction (Hilton et al., 1993). This is also due to a greater incorporation of meteoric water to the hydrothermal convection cells, containing helium of atmospheric isotopic composition. The $^3He/^4He$ data of the La Guitarra deposit thus reflect the incorporation of mantle-derived helium, suggesting that the ultimate source of part of the volatiles contained by mineralizing fluids were cooling magmas. The *R*/Ra values that are lower than those considered to be mantle-derived may be explained by (1) a higher crustal contribution by magma assimilation or deep water/rock interaction, or (2) mixing of the upwelling fluids with air-saturated meteoric waters.

Another process that may mask the occurrence of mantle-derived helium is the fractionation of ^3He to the vapor phase due to boiling. Among the analyzed samples, only one can be considered to be under the influence of boiling: the quartz sample within the interstices of bladed calcite from the stage I silver mineral association. The other samples correspond to (1) mineral associations where boiling was not recorded, as the sphalerite from the base-metal sulfide association of stage I, and the quartz-amethyst from stage IIC late vug lining, or to (2) paragenetic sections that are relatively separated enough in time from evidence of boiling to record the chemical influence of such process upon the resulting solutions, as the quartz from late post-brecciation bands of stage IIB. The petrographic examination of the stage I quartz sample indicates that vapor-rich inclusions were not trapped simultaneously with liquid-rich inclusions, and thus a hypothetical ^3He-rich vapor phase from vapor-rich inclusions could not compensate a ^4He-rich liquid phase from liquid-rich inclusions during the analysis. Hence, given the relatively homogeneous *R*/Ra ratio of the analyzed samples, we may consider that, although the fluids associated with the sample SF96-12 would have had *R*/Ra values similar to those of the other samples, the actually analyzed *R*/Ra can be due to the higher fractionation of the light helium isotope to the vapor phase and its subsequent migration to the surface.

5. The Fe–S–O system after volatile analyses: S_2, O_2 and H_2 fugacities

5.1. Calculation procedure

We constructed a log $f(O_2)$ vs. log $f(S_2)$ diagram at 500 K (Fig. 8) and plotted the volatile analyses from fluid inclusions reported above. The chosen temperature is representative for both temperatures of homogenization in fluid inclusions and mineral geothermometers

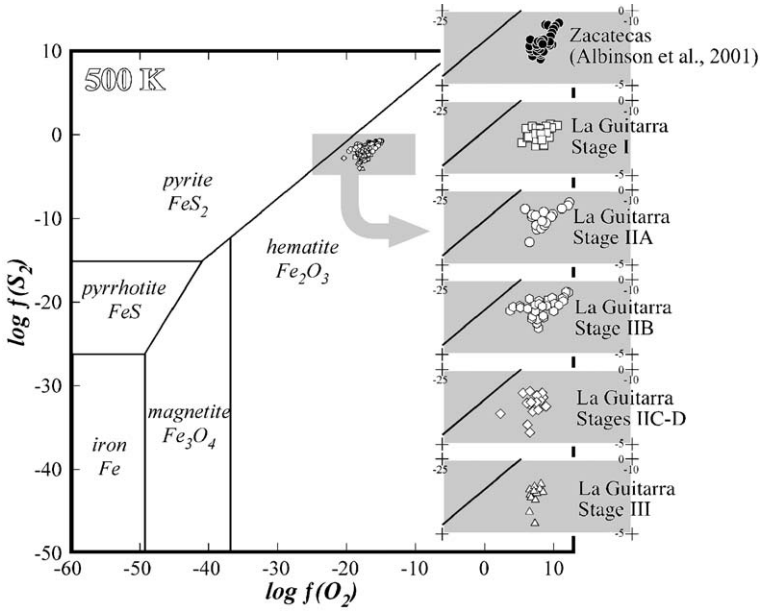

Fig. 8. Correlation diagram between oxygen and sulfur fugacities at 500 K of iron species, with the calculated compositions of mineralizing fluids after single QMS runs for each stage of mineralization at the La Guitarra deposit. The analyses obtained by Albinson et al. (2001) in the Zacatecas deposit were also calculated for comparison.

(Camprubí et al., 2001a,b). To do so we considered the following reactions and equilibrium constants:

$2Fe + S_2(g) \Leftrightarrow 2FeS$ Log Keq $= -\log P_{S_2}(g)$

$3FeS + 2O_2(g) \Leftrightarrow Fe_3O_4 + 3/2S_2(g)$ Log Keq $= \frac{3}{2}\log P_{S_2} - 2\log P_{O_2}$

$3/2Fe + O_2(g) \Leftrightarrow 1/2Fe_3O_4$ Log Keq $= -\log P_{O_2}$

$2Fe_3O_4 + 1/2O_2(g) \Leftrightarrow 3Fe_2O_3$ Log Keq $= -\frac{1}{2}\log P_{O_2}$

$2FeS + S_2(g) \Leftrightarrow 2FeS_2$ Log Keq $= -\log P_{S_2}(g)$

$3FeS_2 + 2O_2 \Leftrightarrow Fe_3O_4 + 3S_2(g)$ Log Keq $= 3\log P_{S_2} - 2\log P_{O_2}$

Log Keq $= 2\log P_{S_2} - \frac{3}{2}\log P_{O_2}$

The expression of equilibrium constants were obtained after

$$\Delta Gr = -RT\ln Keq \quad (1)$$

where R is the constant of gases (8.314 J/mol K), and T is temperature (500 K). ΔGr was calculated using the equation

$$\Delta Gr = \Delta G \text{ products} - \Delta G \text{ reactants} \quad (2)$$

and the free Gibbs energy data at 500 K were obtained from Robie et al. (1928).

We also constructed a log $f(H_2)$ vs. log $f(S_2)$ diagram adding to the above the reaction of water dissociation

$$2H_2O \Leftrightarrow O_2 + 2H_2$$

and proceeded the same way as to construct the log $f(O_2)$ vs. log $f(S_2)$ diagram. The log $f(H_2)$ vs. log $f(S_2)$ diagram is not shown because the calculated fugacity values from the volatile data plotted within the magnetite stability field and that does not correspond to the observed mineralogy of any metallic mineral association from the La Guitarra deposit (see Fig. 15 in Camprubí et al., 2001a). The reason for that discrepancy probably lies in a deficient detection of H_2 during QMS runs.

The sulfur and oxygen fugacities for the analyzed fluid inclusion samples, plotted onto the constructed log $f(O_2)$ vs. log $f(S_2)$ diagram, were calculated from QMS runs after Henry's law

$$f_{gas} = K_{H_{gas}} * X_{gas} \quad (3)$$

where f_{gas} = gas fugacity, $K_{H_{gas}}$ = Henry's constant for the gas, X_{gas} = molar fraction of the gas. The gas concentration values are expressed as mole percents (%mol), defined as

$$\%mol = \frac{\text{gas mol}}{\text{total gas mol}} * 100. \quad (4)$$

At 500 K, Henry's constants (K_H) for H_2 and H_2S are

$$K_{H_{(H_2)}} = 10^{6.057}$$

$$K_{H_{(H_2S)}} = 10^{3.688}$$

and, although the K_H for O_2 at that temperature was not found in the literature, it was deduced from the equation

$$K_{H(O_2)(500\,K)} = K_{H(O_2)(298\,K)} e^{-\frac{\Delta H^{\phi}_{500\,K}}{R}\left(\frac{1}{298} - \frac{1}{T}\right)} \quad (5)$$

where the K_H for O_2 at 298 K is 38800 atm. The reaction heat ($\Delta H°$) for O_2 at 500 K was calculated with

$$\Delta H^{\phi}_{500\,K} = \Delta H^{\phi}_{298\,K} + \int_{298\,K}^{500\,K} \Delta\, Cp\phi \, dT. \quad (6)$$

Following the reaction of water dissociation, if the $\Delta H°$ for the formation of water is 241.81 kJ/mol, then the $\Delta H°$ for oxygen is −241.81 kJ/mol. Then, we substitute the calorific capacity for each chemical species by an expression that is a function of temperature, and Eq. (8) turns to

$$\Delta H^{\phi}_{(500\,K)} = 241.81 \ \text{kJ/molK} + R\left[1.39645 \int_{298}^{500} dT - 4.77 \times 10^{-4} \times \int_{298}^{500} T\, dT - 1.48 \times 10^{-7} \int_{298}^{500} T^2\, dT\right] \quad (7)$$

From Eq. (9) we may calculate the K_H for O_2 at 500 K:

$$K_{H_{(O_2)}} = 10^{-12.676}.$$

As shown in Eq. (3), we may then calculate the respective gas fugacities using Henry's constants at 500 K.

Fig. 8 shows that there are no significant variations in the fugacities of O_2 and S_2 in mineralizing fluids at any stage, and that these are similar to mineralizing fluids in the deposits of the Zacatecas district (Albinson et al., 2001; calculated here for comparison), as all the analyses plot within the same compositional region,

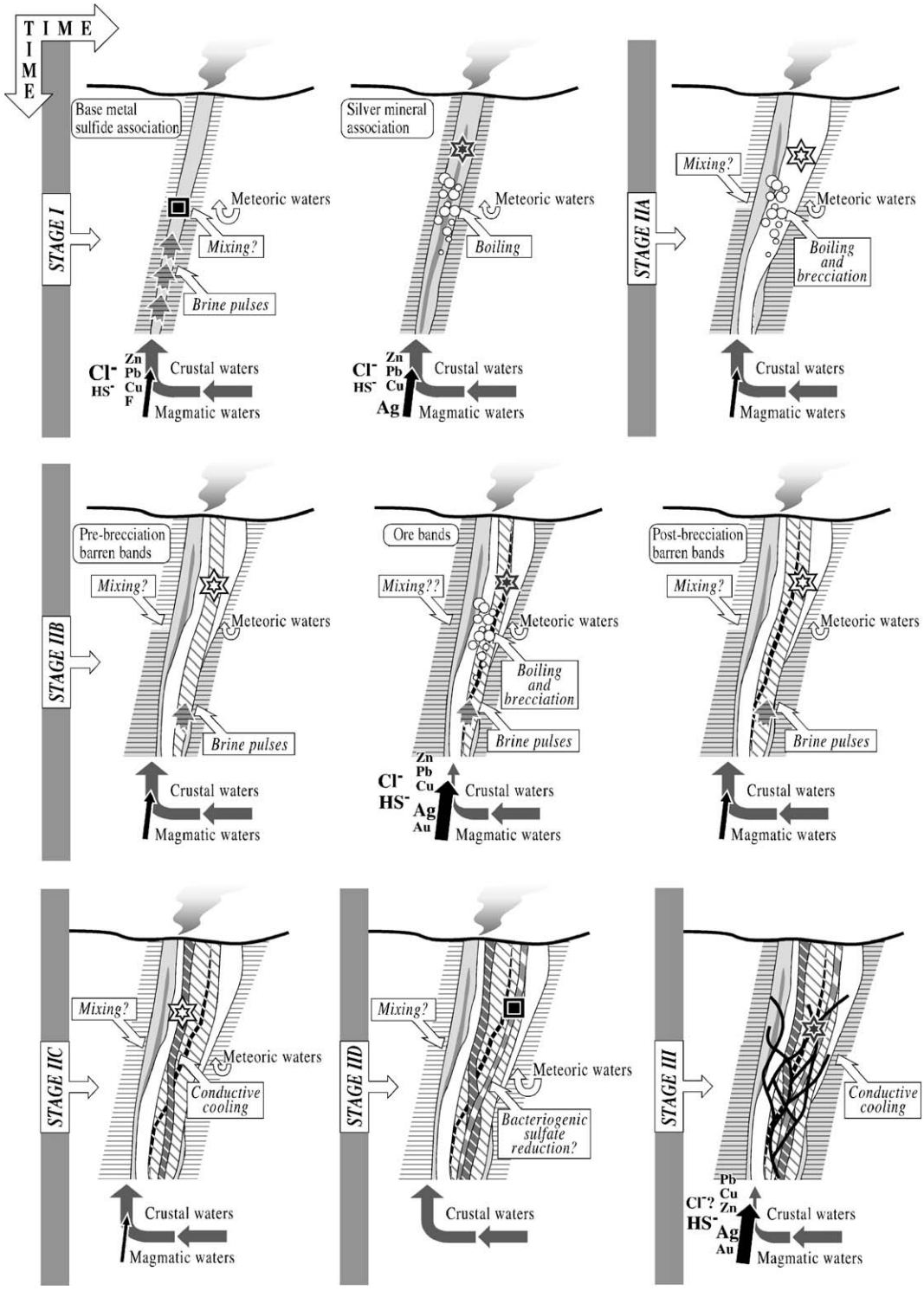

within the hematite stability field and very close to the pyrite stability field. Thus, the mineralizing fluids at the La Guitarra deposit had practically the same "macrochemical" characteristics, and the different styles of mineralization, and the lack or presence of ore associations actually is due to contrasting "microchemical" characteristics.

6. Discussion and conclusions

The sources of mineralizing fluids and the proposed mechanisms of precipitation for the identified mineral associations at the La Guitarra epithermal deposit are summarized in Fig. 9. The conceptual model is in accordance with that proposed by Camprubí et al. (2001b) after petrographic, microthermometric and stable isotope studies. Ore precipitation mechanisms involved boiling, shallow mixing of fluids, conductive cooling and, at a much lesser extent (restricted to stage IID), bacteriogenic sulfate reduction.

Gas analyses from inclusion fluids show the occurrence of three fluid types in all mineralization stages: magmatic, deeply circulated meteoric (crustal waters), and shallow meteoric waters. Volatile compositions that indicate the occurrence of magmatic fluids correlates with He, O and H isotope compositions that also indicate or suggest the occurrence of such source for mineralizing fluids (Fig. 10). Generally speaking, all the analyzed fluids display N_2/Ar ratios suggesting a general composite origin between andesite or rhyolite-derived fluids, and meteoric fluids of any kind. Results from volatile analyses show that shallow waters invaded the system during the waning stages of some hydrothermal pulses, thus confirming the conclusions by Camprubí et al. (2001b) from fluid inclusion and stable isotope data.

The most significant magmatic contributions were found in fluids trapped in sphalerites from the BMSA of stage I (Figs. 2, 7, and 10), in ore-bearing quartz bands of stage IIB (Figs. 4, 7, and 10), and in the sulfosalts from stage III (Figs. 6, 7, and 10). These results are comparable to those found in the study of several Mexican epithermal deposits (Norman et al., 1997b; Albinson et al., 2001). Moreover, the helium isotope analyses show a greater contribution of magmatic fluids in sphalerite than in gangue minerals. Thus, these analyses confirm the occurrence of pulses containing mostly magmatic fluids related to metallic mineralizations in this deposit, either in mineral associations rich in base metals and in associations rich in precious metals. A certain magmatic contribution could also be envisaged in stage IID, although this contradicts the O and H isotopic composition of water (Camprubí et al., 2001b) and does not necessarily imply that there were any magmatic fluid pulses during the formation of stage IID. It is more likely that this magmatic contribution to stage IID is more apparent than actual, as a result of an analytical problem.

Volatile analyses obtained in fluids from stage IIA barren quartz bands (Figs. 3 and 7) and from stage IIB bands (pre- and post-brecciation; Figs. 4 and 7), also point to several sources of hydrothermal fluids, although the magmatic component is more prominent in stage IIB ore-bearing bands.

The evolution of stage IIB may be schematically described as follows. In every case, the indicated components are the major ones but they do not exclude the occurrence of the other:

1. pre-brecciation barren bands precipitated from meteoric waters, mainly crustal,
2. ore-bearing bands precipitated from fluids predominantly magmatic,
3. post-brecciation barren bands precipitated from mixed meteoric, mainly crustal, and magmatic fluids in different proportions, similar to ore-bearing bands, probably recording the influence of the magmatic fluids associated with the main metallic mineralization.

The proposed evolution is in accordance with the $\delta^{18}O_w$ values obtained in a systematic band-to-band stable isotope study carried out on a sample of stage IIB (Camprubí et al., 2001b). In that sample, the lowest

Fig. 9. Cartoon-like representation summarizing the plausible precipitation mechanisms and the relative influx of fluids from several sources for all the stages of mineralization and the most significative mineral associations at the La Guitarra epithermal deposit, as accountable after fluid inclusion microthermometry, stable isotope, volatile and He isotope analyses. The relative importance of the main fluid contributions is intended by the thickness of the arrows that illustrate the incorporation of fluids of different origin into the vein system. White stars represent the lack of metallic mineralization (barren associations), gray stars represent the occurrence of precious metal-bearing associations, and black squares represent the occurrence of base-metal sulfide-bearing associations. The color of striped backgrounds to the veins illustrates the dominance of upwelling fluids (gray), either crustal and magmatic, or descending meteoric waters (white). It also represented the type of metallic mineralization that is present at every mineral association, and the relative abundance of each element by means of the font size. Likewise, the relative abundance and occurrence of chloride (Cl^-) and bisulfide (HS^-) type ligands to the metals within the mineralizing fluids are intended by means of the font size, provided that the occurrence of one does not preclude the occurrence of the other, and is supported by data from microthermometry and H_2S contents in volatiles in fluid inclusions.

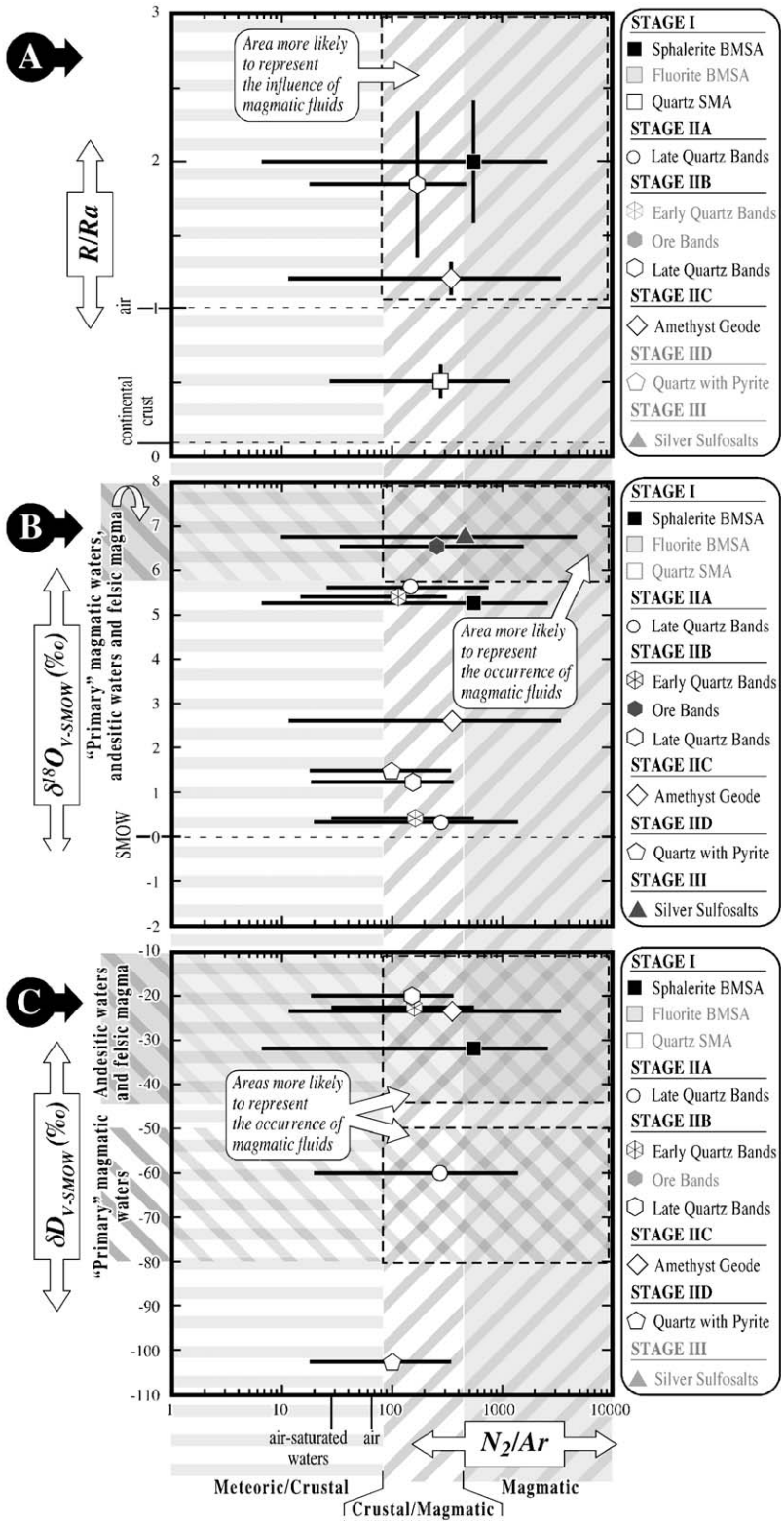
A
B
C
R/Ra
air
continental crust
Area more likely to represent the influence of magmatic fluids
δ18OV-SMOW (‰)
"Primary" magmatic waters, andesitic waters and felsic magma
SMOW
Area more likely to represent the occurrence of magmatic fluids
δDV-SMOW (‰)
Andesitic waters and felsic magma
"Primary" magmatic waters
Areas more likely to represent the occurrence of magmatic fluids
air-saturated waters
air
N2/Ar
Meteoric/Crustal
Crustal/Magmatic
Magmatic
STAGE I
Sphalerite BMSA
Fluorite BMSA
Quartz SMA
STAGE IIA
Late Quartz Bands
STAGE IIB
Early Quartz Bands
Ore Bands
Late Quartz Bands
STAGE IIC
Amethyst Geode
STAGE IID
Quartz with Pyrite
STAGE III
Silver Sulfosalts

$\delta^{18}O_w$ value was obtained in one of the pre-brecciation barren bands (<−2.2‰) and the highest one in the earliest ore-bearing band (+6.3‰), whilst intermediate values were obtained in post-brecciation barren bands.

Data obtained in inclusion fluids from stage III sulfosalts plot within the field of fluids recording some degree of magmatic influence, thus confirming the results obtained in the stable isotope study (Camprubí et al., 2001b). Then, even assuming that mixing between upwelling hydrothermal fluids and shallow meteoric waters occurred, such process was not efficient enough as to induce the ore precipitation during stage III. Considering the specific characteristics of the mineralization of stage III, which is not found in the upper part of the deposit and is apparently confined to the deeper portions of the veins and, furthermore, lacks evidence for boiling, it is proposed that the main mechanism of mineral precipitation during stage III was conductive cooling.

Fig. 7 further illustrates the chemical nature of mineralizing fluids, through the mutual correlations between the H_2S/SO_2, CO_2/CH_4, and N_2/Ar ratios, showing that:

1. ore-bearing associations formed after more oxidized fluids than barren associations (H_2S/SO_2 vs. CO_2/CH_4),
2. the more oxidized fluids are, the more likely is that they come from a magmatic source (N_2/Ar vs. H_2S/SO_2),
3. and ore-bearing associations formed more likely after magmatic fluids (N_2/Ar vs. CO_2/CH_4).

Then, ore-bearing associations preferentially formed after magmatic relatively oxidized fluids whereas barren or poorly mineralized associations preferentially formed after crustal relatively reduced fluids.

The helium isotope analyses display *R*/Ra values between 0.5 and 2, indicating the occurrence of a mantle-derived helium component relatively diluted or "contaminated" by crustal helium. The contribution of magmatic fluids during the precipitation of sphalerite was higher than during the formation of barren associations.

Volatile and helium isotope data are consistent with the conclusions obtained from microthermometric and stable isotope studies by Camprubí et al. (2001b), and suggest that the precious metal-bearing associations at La Guitarra formed after the occurrence of hydrothermal pulses that contained mostly magmatic fluids, and thus it is likely that precious metals were carried by fluids from that source. This does not necessarily mean that precious metals came from the mineralizing fluids exsolved from cooling magmas, as these metals could have been leached at depth by magmatic vapors that condensed and eventually mixed with upwelling magmatic brines. Minerals from base-metal sulfide associations, particularly those in stage I, record both crustal and magmatic sources for mineralizing fluids, thus suggesting that base metals could be derived from deep leaching of crustal rocks.

The positive correlation between an increasing content of magmatic fluids and an increasing relative content of H_2S, similar to other Mexican epithermal deposits with similar mineralogical and geochemical characteristics (Albinson et al., 2001), through N_2/Ar and H_2S/Ar ratios, respectively, suggests that the H_2S necessary to carry gold (and eventually silver) preferentially as bisulfide complexes mostly came from magmatic sources. The chlorine necessary to carry silver and base metals is relatively abundant in inclusion fluids and there is no evidence about its source, although it is plausible that it may also come from magmatic sources, since there are no evaporites or connate brines in the region nearby.

There is no tendency towards either the occurrence of more crustal, more meteoric, nor more magmatic fluids in the formation of the La Guitarra epithermal deposit. This is evidence against any "linear evolution" of the paleohydrothermal system and, alternatively, it is evidence for a pulsing hydrothermal system where each pulse or set of pulses accounts for different compositions of mineralizing fluids. Moreover, these pulses may account for the influx of fluids from distinct reservoirs.

Fig. 10. Correlation diagrams between N_2/Ar and (A) *R*/Ra, (B) $\delta^{18}O$, and (C) δD of mineralizing fluids. The *R*/Ra values are listed in Table 2, and the represented O and H stable isotope values were obtained by Camprubí et al. (2001b). The correlated values came from different aliquots of the same samples in every case. The mineral associations that are not correlated in the diagrams are indicated in grey in the respective key boxes. The black bars within the diagrams represent, (1) for the N_2/Ar ratios, the whole range of data dispersion obtained after single runs, (2) for the *R*/Ra values, the standard deviation (2σ) as reported in Table 2. The symbols used to represent each analyzed sample from a certain mineral association are positioned in the diagrams using the statistical mean value for N_2/Ar ratios, although that mean value does not have any statistical significance and it is used only as an orientative value. In these correlation diagrams N_2/Ar ratios = 0 were skipped, since the absence of N_2 that the corresponding analytical runs recorded do not correspond to an actual lack, but to analytical problems instead; all the analytical runs are reported in the Appendix. The ranges of O and H stable isotopes representing magmatic compositions come from Sheppard et al. (1969), Taylor (1974), and Sheppard (1986) for "primary" magmatic waters, from Taylor (1992) for felsic magmatic waters, and from Giggenbach (1992b,c) for andesitic waters. Key: a.s.w. = air-saturated water, BMSA = base-metal sulfide association, SMA = silver mineral association.

Appendix A. Volatile analyses on stage I samples from the La Guitarra deposit

Sample RSR96-3J, Sphalerite BMSA

Analysis number	5696A	5696B	5696C	5708A	5708B	5708C	5708D	5708E	5708F
H_2	0	0	0.22298	0.34011	0.02063	0.04011	0.02967	0.10963	0.14127
He	0.00128	3.35E−5	0.01171	0.00012	0.00063	0.00100	0.00262	0.00569	0.00142
CH_4	0.00435	0.01328	0.38982	0.03695	0.02564	0.04881	0.07824	0.14295	0.14460
H_2O	999,165	999,709	992,976	994,115	997,771	997,547	997,922	996,030	995,552
N_2	0.00146	0.00756	0.01621	0.03830	0.01132	0.00756	0.01532	0.02168	0.00539
O_2	0.00012	0	0.00080	0	0	0.00027	0.00113	0.00168	0.00196
H_2S	2.94E−5	1.25E−5	0.00030	0.00031	0.00021	0.00023	0.00012	0.00014	3.03E−5
Ar	0.00030	0.00018	8.68E−5	0.00133	0.00029	0.00026	5.57E−5	0.00013	4.51E−5
C_nH_m	0.00021	0.00032	0.00441	7.04E−5	0	2.22E−5	0.00039	0.00164	0.00188
CO_2	0.07565	0.00753	0.05609	0.17109	0.16409	0.14697	0.08014	0.11338	0.14822
SO_2	7.19E−5	0.00015	0	0.00018	2.72E−5	3.84E−5	0.00014	6.08E−5	5.61E−5
N_2/Ar	5	42	187	29	39	29	275	161	120

Sample AM-3, Sphalerite BMSA

Analysis number	5704A	5704B	5704C	5709A	5709B	5709C	5709D	5718A	5718B	5718C
H_2	0	0.14499	0.33740	0	0	0.01662	0.30039	0.27451	0.05639	0.13793
He	0.00160	0.00408	0.00030	0.00852	0.00227	0.00173	0.00626	0.00491	0.00295	0.00291
CH_4	0.04597	0.07038	0.08629	0.06187	0.03728	0.06204	0.06904	0.60933	0.18208	0.42713
H_2O	997,527	995,431	990,555	998,379	998,794	998,322	995,236	990,294	996,786	993,400
N_2	0	0.08704	0.18953	0.01745	0.00644	0.00536	0.00233	0.01485	0.00196	0.01457
O_2	0	0.00215	0.07751	0.00085	0.00046	0.00039	0.00083	0.00056	0.00033	0
H_2S	0	0.00010	0.00037	7.87E−5	8.26E−5	6.83E−5	0.00014	0.00017	5.93E−5	0.00012
Ar	7.53E−6	3.45E−5	0.00474	1.13E−05	7.68E−5	5.09E−6	0.00026	0.00018	4.64E−5	9.70E−5
C_nH_m	0.00031	0.00144	0.00071	0.00047	0.00016	0.00021	0.00025	0.00733	0.00193	0.00404
CO_2	0.19943	0.14675	0.24758	0.07286	0.07370	0.08131	0.09678	0.05889	0.07559	0.07324
SO_2	7.07E−6	2.05E−5	5.88E−5	0	9.32E−5	5.48E−5	0.00014	7.52E−5	0.00010	1.73E−5
N_2/Ar	0	2526	40	1547	84	1053	9	84	42	150

Sample SF96-8B, Fluorite BMSA

Analysis number	5695A	5695B	5695C	5695D	5695E	5717A	5717B	5717C	5717F	5717G	5717H	5717I
H_2	0.03005	0	0	0.04819	0	0.22909	0.54218	0.78342	0.11715	156,279	236,262	127,780
He	0	0.00033	0.00064	0.00623	0.00030	0.00185	0.00694	0.00926	0.00107	0.00710	0.01313	0.00448
CH_4	0.01676	0.02372	0.02695	0.10674	0.03894	0.26127	0.31355	0.31455	0.07881	104,781	125,199	0.89614
H_2O	995,182	995,445	996,241	992,308	992,520	993,761	985,881	981,590	994,615	969,251	959,502	972,652
N_2	0.00883	0.00945	0.01144	0.04949	0.00347	0.00127	0.00237	0.01973	0.03784	0.03348	0.05989	0.02679
O_2	0.00966	0.00868	0.00822	0.02127	0.00622	0.00424	0.00640	0.02633	0.00717	0.01102	0.01664	0.01737
H_2S	0.00011	7.02E−5	9.47E−5	0.00041	1.68E−5	8.81E−5	0	0.00027	1.96E−5	0.00033	0.00071	6.56E−5

Ar	0.00042	0.00010	0.00011	0.00071	0.00027	4.99E−5	9.16E−5	9.90E−5	5.91E−5	0.00044	0.00048	0.00034
C_nH_m	0.00034	0.00053	0.00023	0.00070	0.00081	0.00208	0.00382	0.00327	0.00246	0.01817	0.01986	0.01407
CO_2	0.41563	0.41264	0.32818	0.53547	0.69773	0.12388	0.53623	0.68375	0.29392	0.39416	0.31497	0.49809
SO_2	1.86E−5	1.40E−5	0	0	0.00023	0.00019	0.00043	0.00032	1.72E−5	3.09E−5	5.35E−5	2.28E−5
N_2/Ar	21	92	106	69	13	25	26	199	640	77	126	79

Sample SF96-12, Quartz with bladed calcite SMA

Analysis number	5897A	5897B	5697C	5697E	5697F	5697G	5697H	5697L	5697M	5697N	5697N'
H_2	0.11500	0.74569	0.09037	0.27682	0.02623	0.29089	0.14159	0.06665	0.08793	0.07580	0.37227
He	0.00320	0.00841	0.00106	0.00158	0.00150	0.00188	0.00108	0.00031	0.00390	0.00065	0.00231
CH_4	0.10138	0.63741	0.12158	0.40428	0.10824	0.36181	0.20933	0.14031	0.19834	0.17429	0.40218
H_2O	992,955	980,258	995,311	990,694	996,743	991,282	994,090	995,542	994,865	995,337	989,437
N_2	0.05620	0.09666	0.01785	0.03190	0.00422	0.02043	0.01259	0.01213	0.02868	0.01014	0.02291
O_2	0.00706	0.01020	0	0.00110	0.00059	0.00162	0.00101	0.00160	0.00161	0.00091	0.00061
H_2S	0.00021	0.00021	0.00011	0.00010	0	8.82E−5	0.00012	1.76E−5	0.00025	9.66E−5	0.00013
Ar	0.00206	0.00250	0.00033	3.05E−5	9.39E−6	0.00011	6.37E−5	5.20E−5	6.21E−5	7.10E−5	0.00019
C_nH_m	0.00140	0.01021	0.00125	0.00465	0.00119	0.00443	0.00265	0.00216	0.00267	0.00296	0.00782
CO_2	0.41788	0.46279	0.23615	0.21007	0.18367	0.19055	0.22265	0.22260	0.18996	0.20144	0.24797
SO_2	0.00012	0.00014	0.00022	9.75E−5	6.59E−5	9.75E−5	8.01E−6	4.00E−5	9.48E−5	2.22E−5	5.58E−5
N_2/Ar	27	39	54	1047	450	192	198	233	462	143	122

Appendix B. Volatile analyses on stage IIA samples from the La Guitarra deposit

Sample AM-9A-3, Quartz from post-brecciation bands

Analysis number	5706A	5706B	5706C	5706D	5706E	5706F	5706J	5706K
H_2	0.02279	0.11413	0.04731	0.14028	0.21047	0.01395	0	0.03562
He	0.00160	0.00179	0.00134	0.00248	0.00246	0.00158	0.00216	0.00637
CH_4	0.03945	0.02619	0.06219	0.07047	0.06942	0.05099	0.04260	0.02663
H_2O	998,911	993,480	995,403	993,648	992,385	995,187	998,728	998,150
N_2	0.00102	0.29977	0.09468	0.03956	0.07674	0.04137	0.01593	0.01050
O_2	0	0.02690	0.00750	0.00391	0.00575	0.00586	0.00147	0.00150
H_2S	0.00016	0.00040	0.00012	0.00016	0.00063	7.94E−5	4.97E−5	5.37E−5
Ar	2.25E−5	0.00226	0.00080	0.00150	0.00310	0.00099	2.16E−5	0.00023
C_nH_m	8.34E−5	0.00070	0.00060	0.00092	0.00117	0.00044	0.00045	0.00028
CO_2	0.04374	0.17956	0.24510	0.37566	0.39154	0.36597	0.06445	0.10359
SO_2	4.89E−5	0.00026	7.65E−5	0.00028	0.00023	3.41E−5	3.35E−5	0.00025
N_2/Ar	45	132	118	26	25	42	738	45

(continued on next page)

Appendix B (*continued*)

Sample GB96-1, Quartz from post-brecciation bands

Analysis number	5703A	5703B	5703C	5703D	5703E	5703F	5722A	5722B	5722C	5722G	5722H	5722I	5722J
H_2	0.13418	0.03924	0	0	0.07461	0.28198	0.38061	0.32150	0.17166	200,511	119,135	307,762	454,211
He	0.01291	0.00734	0.00069	0.00378	0.00485	0.01834	0.01662	0.01574	0.01025	0.01972	0.01222	0.02083	0.01806
CH_4	0.10930	0.09959	0.01775	0.11617	0.19883	0.25758	0.23976	0.23616	0.13327	0.86074	0.45945	268,670	506,237
H_2O	994,746	995,549	999,780	996,992	994,417	993,739	988,142	988,658	994,769	963,637	979,869	915,314	885,471
N_2	0.01007	0.00785	0	0.01522	0.03763	0.00718	0.03454	0.03082	0.00906	0.32571	0.07750	153,050	105,481
O_2	0.00297	0.00129	0	0.00041	0.00136	0.00018	0.00063	0.00350	0.00072	0.13892	0.02075	0.52777	0.42165
H_2S	0	0.00037	3.65E−5	6.98E−6	8.96E−5	0.00098	0.00030	5.84E−5	0.00042	0.00102	0.00031	0.00265	0.00171
Ar	0.00029	2.34E−5	5.43E−6	2.00E−5	2.98E−5	0.00010	0.00014	0.00063	3.28E−5	0.00505	0.00049	0.03287	0.01519
C_nH_m	0.00105	0.00098	0.00023	0.00083	0.00124	0.00426	0.00231	0.00185	0.00137	0.01095	0.00536	0.02849	0.06904
CO_2	0.25436	0.28814	0.00327	0.16403	0.23900	0.05415	0.51086	0.52364	0.19606	0.26899	0.24564	0.56097	0.26787
SO_2	0.00026	0.00029	5.30E−5	0.00034	0.00063	0.00141	3.06E−5	0.00034	0.00031	0.00010	6.53E−5	0.00017	0.00010
N_2/Ar	34	335	0	759	1264	70	246	49	276	64	158	47	69

Appendix C. Volatile analyses on stage IIB samples from the La Guitarra deposit

Sample RSR-1E, Quartz from barren post-brecciation bands

Analysis number	5700A	5700B	5700C	5700D	5700E	5700I	5700J	5700K	5700L	5720A	5720B	5720C	5720D	5720G	5720H	5720I
H_2	0.57284	0.54810	0.38866	114,338	400,713	304,346	932,352	156,707	837,638	0.81724	0.80533	0.15794	0.13415	0.75026	156,417	262,076
He	0	0	0	0.00063	0.00130	0	0.00036	0.00179	0.00023	0.01853	0.01994	0.00423	0.00332	0.00876	0.00393	0.02098
CH_4	0.27342	0.42841	0.78285	122,325	357,742	245,873	796,086	113,574	750,265	0.21683	0.35426	0.17492	0.15475	0.83243	141,813	215,971
H_2O	988,572	989,165	985,389	973,089	920,570	835,589	810,198	715,247	832,980	986,771	986,388	992,626	992,813	979,089	965,622	949,097
N_2	0.04373	0.01862	0.03466	0.09728	0.12016	0.55234	0.96840	0.83279	0.43401	0.02715	0.03173	0.04364	0.04080	0.07258	0.08733	0.08018
O_2	0.00290	0.00460	0	0.00114	0.00100	0.30063	0.54308	0.44200	0.21297	0.00325	0.00223	0.00277	0.00667	0.00718	0.00531	0.00047
H_2S	5.80E−5	0.00026	5.90E−5	0.00013	0.00012	0.00205	0.00222	0.00218	0.00057	0.00037	1.00E−5	0.00047	0.00029	0	5.13E−5	0.00082
Ar	0.00098	0.00012	0.00020	0.00044	0.00067	0.00675	0.00270	0.00277	0.00359	0.00041	0.00169	0.00042	0.00112	0.00029	0.00039	0.00040
C_nH_m	0.00283	0.00513	0.00818	0.01843	0.02792	0.05335	0.15189	0.12694	0.14960	0.00364	0.00385	0.00219	0.00220	0.01195	0.01636	0.01657
CO_2	0.24571	0.07832	0.24657	0.20679	0.20785	0.02339	0.02645	0.03866	0.02558	0.23477	0.14212	0.35049	0.35049	0.40783	0.34218	0.19028
SO_2	1.17E−5	5.73E−5	6.92E−5	7.44E−5	0.00013	0.00038	0.00073	0.00011	1.01E−5	0.00076	2.81E−5	0.00032	4.87E−5	6.94E−5	0.00038	0.00055
N_2/Ar	45	151	176	220	179	82	358	301	121	66	19	104	36	253	222	202

Sample RSR-1E, Quartz from barren pre-brecciation bands

Analysis number	5713A	5713B	5713C	5715A	5715B	5715C	5715D	5715E	5715F
H_2	0.80116	0.10764	0.16241	0.27480	0.06013	0.17365	0.06409	0.11716	0.15327
He	0.00978	0.01037	0.01297	0.00045	0.00031	4.89E−5	1.42E−5	0.00021	0.00062
CH_4	0.24278	0.11109	0.12102	0.10774	0.26049	0.19337	0.11794	0.24542	0.91217
H_2O	985,960	989,953	993,663	991,129	994,826	994,267	996,053	993,550	986,268
N_2	0.05279	0.46436	0.09327	0.29881	0.02036	0.02877	0.03129	0.05142	0.04366
O_2	0.00116	0.09179	0.02891	0.00237	0.00274	0.00627	0.00611	0.00540	0.00176
H_2S	0.00010	0.00030	0.00101	0.00062	0	0.00044	0.00046	6.48E−5	2.02E−5

Ar	0.00026	0.00867	0.00139	0.00099	0.00128	0.00109	0.00103	0.00138	0.00016
C_nH_m	0.00410	0.00150	0.00178	0.00801	0.00197	0.00216	0.00081	0.00109	0.00660
CO_2	0.29149	0.20858	0.21015	0.19298	0.16992	0.16718	0.17274	0.22253	0.25499
SO_2	0.00032	0.00040	0.00074	0.00035	0.00018	0.00027	0.00023	0.00027	5.58E−5
N_2/Ar	206	54	67	301	16	26	30	37	276

Sample SF-5B-1, Quartz from barren pre-brecciation bands

Analysis number	5711A	5711B	5711C	5711D	5711E	5711H
H_2	0.65510	0.81809	0.82278	446,676	295,961	140,954
He	0.00638	0.01206	0.00527	0.00807	0.00315	0.01036
CH_4	0.10782	0.10454	0.60966	200,074	248,207	186,223
H_2O	987,867	987,528	975,984	927,056	942,128	964,112
N_2	0.13302	0.04192	0.32035	0.37287	0.15042	0.10226
O_2	0.04243	0.01170	0.23582	0.16215	0.03673	0.00662
H_2S	0.00040	0.00030	0.00107	0.00087	0.00013	4.81E−5
Ar	0.00261	0.00110	0.01088	0.00452	0.00061	0.00019
C_nH_m	0.00086	0.00230	0.00703	0.04839	0.02524	0.00811
CO_2	0.26414	0.25494	0.38849	0.22971	0.12983	0.19035
SO_2	0.00055	0.00021	0.00024	0.00033	5.26E−5	0.00022
N_2/Ar	51	38	29	83	248	526

Sample SF96-3C, Quartz from barren post-brecciation bands

Analysis number	5694A	5694B	5694C	5694D	5694F	5694G	5694H
H_2	0	0	0	0.24596	247,537	435,622	600,536
He	0.00208	0.00085	0.00178	3.81E−5	0.00017	0.00039	0
CH_4	0.04741	0.05413	0.08950	0.42875	187,000	252,950	404,154
H_2O	997,967	998,157	998,031	991,328	952,728	925,804	894,411
N_2	0.03006	0.00072	0.00983	0.00910	0	0.14413	0.20785
O_2	0.00186	0.00068	0.00164	0.00076	0	0.00130	0.00157
H_2S	3.59E−5	4.06E−5	3.58E−5	6.71E−5	0.00017	0.00037	0.00017
Ar	0.00029	3.54E−5	2.10E−5	0.00016	0.00078	0.00054	0.00160
C_nH_m	0.00053	0.00053	0.00087	0.00657	0.03249	0.04517	0.06659
CO_2	0.12201	0.12728	0.09390	0.17594	0.34894	0.24190	0.23569
SO_2	2.05E−5	1.80E−5	1.36E−5	2.52E−5	7.99E−5	8.52E−5	7.97E−5
N_2/Ar	105	20	469	58	0	266	103

Sample AM96-4, Quartz, sulfides and sulfosalts from ore bands

Analysis number	5710A	5710B	5710C	5710D	5710E	5710F	5719A	5719B	5719C	5719D	5719H	5719I	5719J
H_2	0	0.01808	0	0	0	0	0	0	0	0.00052	0	0.05117	0.15983
He	0.00048	0	0.00013	0.00034	0.00033	0.00149	0.00358	0.00188	0.00274	0.00409	0.00187	0.00369	0.00715
CH_4	0.03325	0.01874	0.02110	0.02852	0.03176	0.05971	0.02968	0.02882	0.02282	0.03733	0.06722	0.17034	0.21122
H_2O	997,081	994,324	995,325	995,280	995,069	993,810	997,662	994,959	995,420	994,695	993,142	992,491	990,065

(continued on next page)

Appendix C (*continued*)

Sample AM96-4, Quartz, sulfides and sulfosalts from ore bands													
Analysis number	5710A	5710B	5710C	5710D	5710E	5710F	5719A	5719B	5719C	5719D	5719H	5719I	5719J
N_2	0.02718	0.01082	0.01548	0.01117	0.01346	0.01890	0.03916	0.01490	0.01095	0.01179	0.02941	0.01681	0.01781
O_2	2.40E−5	8.26E−5	0	0	1.37E−5	0	0.00033	0	8.40E−5	0	0.00148	0.00075	0.00269
H_2S	0.00024	0.00027	0.00015	0.00011	0.00014	0.00017	0.00019	8.50E−5	0.00022	0.00023	0.00014	5.67E−5	0.00039
Ar	1.98E−5	0.00033	0.00018	0.00011	2.79E−5	9.29E−5	0.00051	0.00022	7.37E−5	7.38E−5	0.00017	7.86E−5	0.00010
C_nH_m	0.00083	0.00087	0.00059	0.00059	0.00068	0.00103	0.00067	0.00076	0.00063	0.00076	0.00112	0.00327	0.00429
CO_2	0.22980	0.51909	0.42972	0.43105	0.44656	0.53749	0.15947	0.45743	0.42042	0.47565	0.58432	0.50478	0.59004
SO_2	2.60E−5	0.00032	9.11E−5	7.88E−5	8.13E−5	0.00011	0.00022	1.68E−5	2.01E−5	3.91E−5	1.95E−5	3.78E−5	7.62E−5
N_2/Ar	1369	33	85	99	482	203	77	68	148	160	168	214	173

Appendix D. Volatile analyses on stages IIC and IID samples from the La Guitarra deposit

Sample SF96-2, Quartz-amethyst lining vugs, stage IIC										
Analysis number	5714A	5714B	5714C	5714D	5714E	5714F	5714J	5714K	5714L	5714M
H_2	0.67490	111,037	0.19888	0.15221	0.06519	0.04264	133,364	494,001	470,353	456,057
He	0.00888	0.01098	0.00479	0.00413	0.00280	0.00358	0.00386	0.00670	0.00540	0.01184
CH_4	0.06606	0.33766	0.12752	0.10228	0.11188	0.12152	123,925	611,616	551,494	560,881
H_2O	991,136	985,042	996,329	997,277	997,710	998,127	972,892	886,608	895,273	894,285
N_2	0.00934	0.01578	0.00826	0.00153	0.00619	0.00159	0.05046	0.14834	0.13295	0.17111
O_2	0.00243	0.00052	0.00065	0.00031	0.00085	0.00210	0.00171	0.00015	0.00052	0
H_2S	3.82E−5	0.00062	0.00012	0.00011	2.99E−5	0	0.00012	0.00047	1.29E−6	0.00021
Ar	0.00048	0.00017	2.27E−5	6.39E−7	9.48E−5	0.00014	0.00049	0.00144	0.00161	0.00260
C_nH_m	0.00043	0.00714	0.00094	0.00077	0.00014	0.00021	0.02036	0.05995	0.06713	0.10852
CO_2	0.12384	0.01213	0.02567	0.01077	0.04177	0.01551	0.06112	0.06733	0.04813	0.10986
SO_2	3.59E−5	0.00059	0.00026	0.00022	4.57E−5	8.38E−5	0.00023	0.00023	6.78E−5	0.00062
N_2/Ar	20	92	364	2401	65	11	103	103	83	66

Sample LC-9B, Quartz from stage IID										
Analysis number	5702A	5702B	5702C	5702D	5702E	5702F	5702G	5702K	5702L	5702M
H_2	0.14207	0	0.18852	0.02531	0.07656	0	0.04010	0.13421	0.04123	0.32024
He	0	3.16E−5	0	0	0	0	0	0	0	0
CH_4	0.11803	0.03304	0.13186	0.11429	0.20235	0.06369	0.11143	0.43959	0.16584	0.61698
H_2O	996,095	998,286	996,441	994,492	994,345	996,912	993,650	989,468	993,513	989,845
N_2	0.02535	0.01629	0.00865	0.04058	0.05489	0.02057	0.01459	0.02588	0.01603	0.02651
O_2	0.00510	2.57E−6	0.00439	0.00632	0.01035	0.00048	0.00276	0.00191	0.00033	0.00384
H_2S	0.00048	2.13E−5	0.00027	0.00025	6.44E−5	8.92E−5	0.00020	0.00033	4.16E−6	0.00015
Ar	0.00060	0.00085	0.00037	0.00062	0.00108	0.00030	0.00015	7.98E−5	0.00014	0.00014
C_nH_m	0.00144	0.00047	0.00044	0.00050	0.00159	0.00046	0.00070	0.00332	0.00133	0.00579
CO_2	0.09730	0.12068	0.02126	0.36281	0.21859	0.22317	0.46502	0.44785	0.42376	0.04187
SO_2	0.00014	3.73E−5	8.96E−5	8.01E−5	2.94E−5	5.49E−5	8.97E−5	7.65E−5	3.65E−5	9.75E−5
N_2/Ar	42	19	23	65	51	68	98	324	116	191

Appendix E. Volatile analyses on stage III samples from the La Guitarra deposit

Sample RSR-1D, Silver sulfosalts in small veins															
Analysis number	5699A	5699B	5699C	5699D	5699E	5699F	5712A	5712B	5712C	5712D	5712E	5721A	5721B	5721C	5721D
H_2	0.12756	0.02708	0.12180	0	0.00311	0	0.07236	0	0.12360	0	0.01539	0.08686	0.30884	0.07739	0.04105
He	0	0	0.00841	0.00176	0.00357	0	0.00421	0.00164	0.01385	0.00286	0.00453	0.00353	0.00797	0.00412	0.00235
CH_4	0.03191	0.03718	0.07226	0.05377	0.09092	0.03075	0.07637	0.04402	0.09744	0.09295	0.15360	0.12989	0.38892	0.22017	0.10652
H_2O	987,488	992,034	986,195	993,334	990,121	992,612	990,729	992,625	987,278	991,973	989,990	991,346	982,112	988,811	991,993
N_2	0.24128	0.05392	0.11901	0.02153	0.03657	0.00693	0.01822	0.01728	0.11219	0.03063	0.03154	0.00830	0.00077	0	0
O_2	0.00382	0.00193	0.00263	0.00053	0.00034	0.00089	0.00128	0.00044	0.00083	0.00037	0.00067	0	0	0.00033	0.00092
H_2S	0.00016	0.00022	0.00056	0.00013	0.00023	1.47E−6	0.00014	7.38E−5	0.00037	0.00011	0.00022	0.00053	0.00065	7.53E−6	4.97E−5
Ar	0.00184	0.00030	0.00057	0.00013	0.00014	1.67E−5	0.00015	1.26E−5	8.87E−5	3.51E−5	4.23E−5	2.62E−5	9.78E−5	4.31E−5	3.69E−5
C_nH_m	0.00096	0.00072	0.00251	0.00088	0.00142	0.00070	0.00126	0.00088	0.00277	0.00146	0.00238	0.00109	0.00407	0.00179	0.00154
CO_2	0.84345	0.67508	105,261	0.58788	0.85151	0.69952	0.75289	0.67307	0.92094	0.67417	0.79244	0.63498	107,754	0.81512	0.64818
SO_2	0.00024	0.00014	0.00017	3.63E−5	7.31E−5	7.59E−5	0.00017	0.00012	0.00015	8.72E−5	0.00015	0.00021	0.00071	9.93E−5	0.00022
N_2/Ar	131	178	208	163	252	414	120	1368	1265	873	746	317	8	0	0

Appendix F. Fugacity values, as calculated after QMS analyses in fluid inclusions at the La Guitarra deposit (this study), and Zacatecas (Albinson et al., 2001)

			log f H_2	log f O_2	log f H_2S
Stage I	Sample RSR96-3J, Sphalerite BMSA	5696A		−18.60	−2.84
		5696B			−3.22
		5696C	3.41	−17.77	−1.83
	La Guitarra	5708A	3.59		−1.82
		5708B	2.37		−1.99
		5708C	2.66	−18.24	−1.95
		5708D	2.53	−17.62	−2.23
		5708E	3.10	−17.45	−2.17
		5708F	3.21	−17.38	−2.83
	Sample AM-3, Sphalerite BMSA	5704A			
		5704B	3.22	−17.34	−2.31
		5704C	3.59	−15.79	−1.74
	La Guitarra	5709A		−17.75	−2.42
		5709B		−18.01	−2.40
		5709C	2.28	−18.08	−2.48
		5709D	3.53	−17.76	−2.17
		5718A	3.50	−17.93	−2.08
		5718B	2.81	−18.16	−2.54

(continued on next page)

Appendix F (*continued*)

			log f H_2	log f O_2	log f H_2S
		5718C	3.20		−2.23
	Sample SF96-8B, Fluorite BMSA	5695A	2.53	−16.69	−2.27
		5695B		−16.74	−2.47
		5695C		−16.76	−2.34
	La Guitarra	5695D	2.74	−16.35	−1.70
		5695E		−16.88	−3.09
		5717A	3.42	−17.05	−2.37
		5717B	3.79	−16.87	
		5717C	3.95	−16.26	−1.88
		5717F	3.13	−16.82	−3.02
		5717G	4.25	−16.63	−1.79
		5717H	4.43	−16.45	−1.46
		5717I	4.16	−16.44	−2.50
	Sample SF96-12, Quartz with bladed calcite SMA	5897A	3.12	−16.83	−1.99
		5897B	3.93	−16.67	−1.99
		5697C	3.01		−2.27
		5697E	3.50	−17.63	−2.31
	La Guitarra	5697F	2.48	−17.91	
		5697G	3.52	−17.47	−2.37
		5697H	3.21	−17.67	−2.23
		5697L	2.88	−17.47	−3.07
		5697M	3.00	−17.47	−1.91
		5697N	2.94	−17.72	−2.33
		5697N’	3.63	−17.89	−2.20
Stage IIA	Sample AM-9A-3, Quartz from post-brecciation bands	5706A	2.41		−2.11
		5706B	3.11	−16.25	−1.71
	La Guitarra	5706C	2.73	−16.80	−2.23
		5706D	3.20	−17.08	−2.11
		5706E	3.38	−16.92	−1.51
		5706F	2.20	−16.91	−2.41
		5706J		−17.51	−2.62
		5706K	2.61	−17.50	−2.58
	Sample GB96-1, Quartz from post-brecciation bands	5703A	3.18	−17.20	
		5703B	2.65	−17.57	−1.74
		5703C			−2.75
	La Guitarra	5703D		−18.06	−3.47
		5703E	2.93	−17.54	−2.36
		5703F	3.51	−18.42	−1.32
		5722A	3.64	−17.88	−1.83
		5722B	3.56	−17.13	−2.55
		5722C	3.29	−17.82	−1.69
		5722G	4.36	−15.53	−1.30
		5722H	4.13	−16.36	−1.82

		5722I	4.55	−14.95	−0.89
		5722J	4.71	−15.05	−1.08
Stage IIB	Sample RSR-1E, Quartz from barren post-brecciation bands	5700A	3.82	−17.21	−2.55
		5700B	3.80	−17.01	−1.90
		5700C	3.65		−2.54
	La Guitarra	5700D	4.12	−17.62	−2.20
		5700E	4.66	−17.68	−2.23
		5700I	4.59	−15.15	−0.95
		5700J	5.03	−14.94	−0.97
		5700K	5.25	−15.03	−0.97
		5700L	4.98	−15.35	−1.56
		5720A	3.97	−17.16	−1.74
		5720B	3.96	−17.33	−3.31
		5720C	3.26	−17.23	−1.64
		5720D	3.18	−16.85	−1.85
		5720G	3.93	−16.82	
		5720H	4.25	−16.95	−2.60
		5720I	4.48	−18.00	−1.40
	Sample RSR-1E, Quartz from barren pre-Brecciation bands	5713A	3.96	−17.61	−2.31
		5713B	3.09	−15.71	−1.83
		5713C	3.27	−16.21	−1.31
		5715A	3.50	−17.24	−1.52
	La Guitarra	5715B	2.84	−17.38	
		5715C	3.30	−16.88	−1.67
		5715D	2.86	−16.89	−1.65
		5715E	3.13	−16.94	−2.50
		5715F	3.24	−17.43	−3.01
	Sample SF-5B−1, Quartz from barren pre-brecciation bands	5711A	3.87	−16.05	−1.71
		5711B	3.97	−16.61	−1.83
		5711C	3.97	−15.30	−1.28
		5711D	4.71	−15.47	−1.37
	La Guitarra	5711E	4.53	−16.11	−2.20
		5711H	4.21	−16.86	−2.63
	Sample SF96-3C, Quartz from barren post-brecciation bands	5694A		−17.41	−2.76
		5694B		−17.84	−2.70
		5694C		−17.46	−2.76
		5694D	3.45	−17.80	−2.49
	La Guitarra	5694F	4.45		−2.08
		5694G	4.70	−17.56	−1.74
		5694H	4.84	−17.48	−2.08
	Sample AM96-4, Quartz, sulfides and sulfosalts from ore bands	5710A		−19.30	−1.93
		5710B	2.31	−18.76	−1.88
		5710C			−2.14
		5710D			−2.27
	La Guitarra	5710E		−19.54	−2.17

(continued on next page)

Appendix F (*continued*)

			log f H_2	log f O_2	log f H_2S
		5710F			−2.08
		5719A		−18.16	−2.03
		5719B			−2.38
		5719C		−18.75	−1.97
		5719D	0.77		−1.95
		5719H		−17.51	−2.17
		5719I	2.77	−17.80	−2.56
		5719J	3.26	−17.25	−1.72
Stage IICD	Sample SF96-2, Quartz–amethyst lining vugs, stage IIC	5714A	3.89	−17.29	−2.73
		5714B	4.10	−17.96	−1.52
	La Guitarra	5714C	3.36	−17.86	−2.23
		5714D	3.24	−18.18	−2.27
		5714E	2.87	−17.75	−2.84
		5714F	2.69	−17.35	
		5714J	4.18	−17.44	−2.23
		5714K	4.75	−18.50	−1.64
		5714L	4.73	−17.96	−4.20
		5714M	4.72		−1.99
	Sample LC-9B, Quartz from stage IID	5702A	3.21	−16.97	−1.63
		5702B		−20.27	−2.98
		5702C	3.33	−17.03	−1.88
	La Guitarra	5702D	2.46	−16.88	−1.91
		5702E	2.94	−16.66	−2.50
		5702F		−17.99	−2.36
		5702G	2.66	−17.24	−2.01
		5702K	3.18	−17.39	−1.79
		5702L	2.67	−18.16	−3.69
		5702M	3.56	−17.09	−2.14
Stage III	Sample RSR-1D, Silver sulfosalts in small veins	5699A	3.16	−17.09	−2.11
		5699B	2.49	−17.39	−1.97
	La Guitarra	5699C	3.14	−17.26	−1.56
		5699D		−17.95	−2.20
		5699E	1.55	−18.14	−1.95
		5699F		−17.73	−4.14
		5712A	2.92	−17.57	−2.17
		5712B		−18.03	−2.44
		5712C	3.15	−17.76	−1.74
		5712D		−18.11	−2.27
		5712E	2.24	−17.85	−1.97
		5721A	3.00		−1.59
		5721B	3.55		−1.50
		5721C	2.95	−18.16	−3.44
		5721D	2.67	−17.71	−2.62

Stage I	Sample Veta Grande 93-1 stage I (quartz+sulfide)	5472A	2.89	−17.43	−1.90
		5472B	2.90	−18.06	−2.42
	Zacatecas	5472C	3.01	−16.32	−2.11
		5472D	2.77	−17.85	−2.56
		5472E	2.98	−17.44	−2.20
		5472I	3.09	−17.24	−2.63
		5472J	2.26	−17.11	−2.56
		5472K	2.98	−18.09	−2.20
		5472L	3.15	−17.25	−2.47
		5472M	2.91	−17.01	−2.31
		5472N	3.13	−16.91	−2.31
		5472O	3.00	−16.97	−2.06
		5472P	3.79	−17.13	−2.65
		5472Q	3.51	−16.78	−2.11
		5472R	3.77	−16.68	−0.87
	Bote 88-2-3: Cantera vein outcrop amethyst	5445A	2.58	−16.55	−2.17
		5445B	2.65	−16.52	−2.17
		5445C	2.68	−17.86	−2.86
		5445D	2.62	−17.33	−2.36
	Zacatecas	5445E	2.19	−17.14	−2.27
		5445I	2.71	−17.44	−2.59
		5445J	2.63	−17.54	−2.14
	Bote 88-3-2: Cantera vein outcrop (quartz and sulfides)	5468A	3.12	−17.19	−2.34
		5468B	3.26	−17.17	−2.60
		5468C	3.25	−17.21	−3.06
	Zacatecas	5468F	3.49	−17.43	−2.54
		5468G	3.43	−16.87	−2.14
		5468H	4.10	−17.43	−2.49
	Veta Grande 90-1-A: −375 m level Veta Grande mine (sphalerite)	5423A	2.90	−17.17	−1.97
		5423B	4.10	−15.81	−0.71
		5423C	3.67	−16.23	−1.13
		5423D	3.36	−16.57	−1.81
		5423E	3.69	−16.86	−0.82
	Zacatecas	5423F	3.76	−16.47	−1.57
		5423J	3.67	−16.63	−0.85
		5423K	3.79	−16.35	−1.35
		5423L	3.79	−16.35	−1.35
		5423M	3.89	−16.10	−0.93
	Veta Grande 90-1-A: −375 m level I45	5405A	2.46	−16.76	−1.91
		5405B	3.40	−16.65	−2.08
	Grande mine (calcite)	5405C	2.74	−17.02	−2.36
		5405D	2.80	−17.07	−2.27

(continued on next page)

Appendix F (*continued*)

			log f H_2	log f O_2	log f H_2S
		5405E	3.59	−16.61	−1.95
	Zacatecas	5405F	2.51	−16.98	−2.58
		5405K	3.50	−16.90	−2.03
		5405L	3.27	−17.24	−2.44
		5405M	3.66	−17.18	−2.54
		5405N	3.59	−17.06	−2.36
		5405O	3.61	−17.20	−2.50
		5405P	4.34	−17.27	−2.27
		5405Q	3.49	−16.86	−2.17
Stage III	Veta Grande 93-1 surface (quartz)	5456A	3.13	−17.13	−1.78
		5456B	2.56	−16.53	−1.91
		5456C	3.04	−16.81	−1.97
	Zacatecas	5456D	2.67	−17.19	−1.93
		5456E	3.13	−17.22	−2.77
		5456F	2.94	−17.02	−1.79
		5456I	3.84	−16.87	−1.91
		5456J	3.21	−18.03	−1.78
Stage IV		5457A	2.43	−17.49	−2.27
		5457B	2.57	−17.19	−2.64
	Zacatecas	5457C	2.90	−17.06	−2.01
		5457D	3.17	−17.04	−2.08
		5457E	3.27	−16.99	−1.77

Acknowledgements

Most of this paper and the conclusions therein are part of the Ph.D. research of A. Camprubí. Financial support for this study was initially received from the European Union Research Fund through contract cI1∗-ct94-0075 (dg 12 hsmu). Further support was received through Mexico funded projects J32506-T and 46473-F (CONACyT) and IN122604 (PAPIIT-DGAPA). Logistic assistance during field work was provided by the mining company formerly known as Luismin S.A. de C.V., fundamentally through Román Torres, Ricardo Flores and Jesús Rosales and the staff at Temascaltepec (1995–1998). A. Camprubí also thanks Robert Nartey for his hospitality at Socorro during the QMS analyses. Some QMS runs were actually assisted by Erika Maschmeyer. Rosa M. Prol-Ledesma kindly assisted us in this paper and from the very beginning of our research, and her help has been fundamental during the last stages of the elaboration of this manuscript. The manuscript has also greatly benefited from the critical reviews and suggestions of two anonymous referees, and an anonymous editor. **[DR]**

References

Aiken, C.L.V., Schellhorn, R.W., de la Fuente, M.F., 1988. Gravity of northern Mexico. In: Clark, K.F., Goodell, P.C., Hoffer, J.M. (Eds.), Stratigraphy, Tectonics, and Resources of Parts of Sierra Madre Occidental Province. El Paso Geological Society, Field Conference Guidebook, pp. 119–133.

Albinson, T., Norman, D.I., Cole, D., Chomiak, B.A., 2001. Controls on formation of low-sulfidation epithermal deposits in Mexico: constraints from fluid inclusion and stable isotope data. In: Albinson, T., Nelson, C.E. (Eds.), New Mines and Discoveries in Mexico and Central America. Society of Economic Geologists Special Publication Series, vol. 8, pp. 1–32.

Ballantine, C.J., Burgess, R., Marty, B., 2002. Tracing fluid origin, transport and interaction in the crust. In: Porcelli, D., Ballantine, C. J., Wieler, R. (Eds.), Noble Gases In Geochemistry and Comochemistry. . Reviews in Mineralogy and Geochemistry, 47. Mineralogical Society of America, pp. 539–614.

Benton, L.D., 1991. Composition and source of the hydrothermal fluids of the Santo Niño vein, Fresnillo, Mexico, as determined from $^{87}Sr/^{86}Sr$, stable isotope, and gas analyses: M.Sc. thesis, New Mexico Institute of Mining and Technology, Socorro NM. 55 pp.

Blatter, D.L., Carmichael, I.S.E., Deino, A.L., Renne, P.R., 2001. Neogene volcanism at the front of the central Mexican volcanic belt: basaltic andesites to dacites, with contemporaneous shoshonites and high-TiO_2 lava. Geologic Society of America Bulletin 113, 1324–1342.

Camprubí, A., Canals, À., Cardellach, E., Prol-Ledesma, R.M., Rivera, R., 2001a. The La Guitarra Ag–Au low sulfidation epithermal deposit, Temascaltepec district, Mexico: vein structure, mineralogy, and sulfide–sulfosalt chemistry. In: Albinson, T., Nelson, C.E. (Eds.), New Mines and Discoveries in Mexico and Central America. Society of Economic Geologists Special Publication Series, vol. 8, pp. 133–158.

Camprubí, A., Cardellach, E., Canals, À., Lucchini, R., 2001b. The La Guitarra Ag–Au low sulfidation epithermal deposit, Temascaltepec district, Mexico: fluid inclusion and stable isotope data. In: Albinson, T., Nelson, C.E. (Eds.), New Mines and Discoveries in Mexico and Central America. Society of Economic Geologists Special Publication Series, vol. 8, pp. 159–186.

Camprubí, A., Ferrari, L., Cosca, M.A., Cardellach, E., Canals, À., 2003. Ages of epithermal deposits in Mexico: regional significance and links with the evolution of Tertiary volcanism. Economic Geology 98 (5), 1029–1037.

Cooke, D.R., Bloom, M.S., 1990. Epithermal and subjacent porphyry mineralization, Acupan, Baguio District, Philippines: a fluid-inclusion and paragenetic study. In: Hedenquist, J.W., White, N.C., Siddeley, G. (Eds.), Epithermal Gold Mineralization of the Circum-Pacific: Geology, Geochemistry, Origin and Exploration, I. Journal of Geochemical Exploration, vol. 35, pp. 297–340.

Einaudi, M.T., Hedenquist, J.W., Inan, E.E., 2003. Sulfidation state of fluids in active and extinct hydrothermal systems: transitions from porphyry to epithermal environments. In: Simmons, S.F., Graham, I. (Eds.), Volcanic, Geothermal, and Ore-Forming Fluids: Rulers and Witnesses of Processes within the Earth. Society of Economic Geologists, Special Publication Series, vol. 10, pp. 285–313.

Ferrari, L., López-Martínez, M., Rosas-Elguera, J., 2002. Ignimbrite flare up and deformation in the southern Sierra Madre Occidental, western Mexico: implications for the late subduction history of the Farallon plate. Tectonics 21, 17-1/24.

Giggenbach, W.F., 1992a. The composition of gases in geothermal and volcanic systems as a function of tectonic setting. Proceedings 7th International Symposium on Water–Rock Interaction (WRI-7). A. A. Balkema, Rotterdam, pp. 873–878.

Giggenbach, W.F., 1992b. Magma degassing and mineral deposition in hydrothermal systems along convergent plate boundaries. Economic Geology 87, 1927–1944.

Giggenbach, W.F., 1992c. Isotopic shifts in waters from geothermal and volcanic systems along convergent plate boundaries and their origin. Earth and Planetary Science Letters 113, 495–510.

Giggenbach, W.F., Poreda, R.J., 1993. Helium isotopic and chemical composition of gases from volcanic–hydrothermal systems in the Philippines. Geothermics 22, 369–380.

Giggenbach, W.F., Sano, Y., Wakita, H., 1994. Isotopic composition of helium and CO_2 and CH_4 contents in gases produced along the New Zealand part of a convergent plate boundary. Geochimica et Cosmochimica Acta 57, 3427–3455.

Gomberg, J., Priestley, K.F., Masters, T.G., Brune, J.N., 1988. The structure of the crust and upper mantle of northern Mexico. Geophysical Journal of the Royal Astronomical Society 94, 1–20.

Hedenquist, J.W., Aoki, M., 1991. Meteoric interaction with magmatic discharges in Japan and the significance of mineralization. Geology 19, 1041–1044.

Hilton, D.R., Craig, H., 1989. A helium isotope transect along the Indonesian archipelago. Nature 342, 906–908.

Hilton, D.R., Hammerschmidt, K., Teufel, S., Friedrichsen, H., 1993. Helium isotope characteristics of Andean geothermal fluids and lavas. Earth and Planetary Science Letters 120, 265–282.

Molina-Garza, R., Urrutia-Fucugauchi, J., 1993. Deep crustal structure of central Mexico derived from interpretation of Bouguer gravity anomaly data. Journal of Geodynamics 17, 181–201.

Moore, J.N., Norman, D.I., Kennedy, B.M., 2001. Fluid inclusion gas compositions from an active magmatic–hydrothermal system: a

case study of The Geysers geothermal fluids, USA. Chemical Geology 173, 3–30.

Morán-Zenteno, D.J., Corona-Chávez, P., Tolson, G., 1996. Uplift and subduction erosion in southwestern Mexico since the Oligocene: pluton geobarometry constraints. Earth and Planetary Science Letters 141, 51–65.

Morán-Zenteno, D.J., Tolson, G., Martínez-Serrano, R.G., Martiny, B., Schaaf, P., Silva-Romo, G., Macías-Romo, C., Alba-Aldave, L., Hernández-Bernal, M.S., Solís-Pichardo, G.N., 1999. Tertiary arc-magmatism of the Sierra Madre del Sur, Mexico, and its transition to the volcanic activity of the Trans-Mexican Volcanic Belt. Journal of South American Earth Sciences 12, 513–535.

Nava, A., Núñez-Cornú, F., Córdoba, D., Mena, M., Ansorge, J., González, J., Rodríguez, M., Banda, M., Mueller, S., Udías, M., García-García, M., Calderón, G., 1988. Structure of the Middle America trench in Oaxaca, Mexico. Tectonophysics 154, 541–553.

Nier, A.O., Schlutter, D.J., 1985. High-performance double focusing mass spectrometer. Review of Scientific Instruments 56, 214–219.

Norman, D.I., Musgrave, J.A., 1994. N_2–Ar–He compositions in fluid inclusions: indicators of fluid source. Geochimica et Cosmochimica Acta 58, 1119–1131.

Norman, D.I, Moore, J.N., Musgrave, J.A., 1997a. Gaseous species as tracers in geothermal systems. Proceedings 22nd Workshop on Geothermal Reservoir Engineering, Stanford University, California, Jan. 27–29.

Norman, D.I, Chomiak, B., Albinson, T., Moore, J.N., 1997b. Volatiles in epithermal systems: the big picture. GSA 1997 Annual Meeting, Abstracts with Programs, vol. A-206.

Patterson, D.B., Honda, M., McDougall, I., 1994. Noble gases in mafic phenocrysts and xenoliths from New Zealand. Geochimica et Cosmochimica Acta 58, 4411–4427.

Patterson, D.B., Farley, K.A., McInnes, B.I.A., 1997. Helium isotopic composition of the Tabar-Lihir-Tanga-Feni island arc, Papua New Guinea. Geochimica et Cosmochimica Acta 61, 2485–2496.

Poreda, R., Craig, H., 1989. Helium isotope ratios in Circum-Pacific volcanic arcs. Nature 338, 473–478.

Robie, R.A., Hemingway, B.S., Fisher, J.R., 1928. Thermodynamic properties of minerals and related substances at a 1 bar (10^5 pascals) pressure and at higher temperatures. U.S. Geological Survey Bulletin 1452 (456 pp.).

Schellhorn, R.W., Aiken, C.L.V., de la Fuente, M.F., 1991. Bouguer gravity anomalies and crustal structure in northwestern Mexico. In: Dauphin, J.P., Simonet, B.R.T. (Eds.), The Gulf and Peninsular Province of the Californias. AAPG Memoir, vol. 47, pp. 197–215.

Sheppard, S.M.F., 1986. Characterization and isotopic variation in natural waters. In: Ribbe, P.H. (Ed.), Stable Isotopes in High Temperature Geological Processes. Mineralogical Society of America, vol. 16, pp. 1–40.

Sheppard, S.M.F., Nielsen, R.L., Taylor Jr., H.P., 1969. Oxygen and hydrogen isotope ratios of clay minerals from porphyry copper deposits. Economic Geology 64, 755–777.

Sillitoe, R.H., Hedenquist, J.W., 2003. Linkages between volcanotectonic settings, ore-fluid compositions, and epithermal precious metal deposits. In: Simmons, S.F., Graham, I. (Eds.), Volcanic, Geothermal, and Ore-Forming Fluids: Rulers and Witnesses of Processes within the Earth. Society of Economic Geologists, Special Publication Series, vol. 10, pp. 315–343.

Simmons, S.F., 1995. Magmatic contributions to low-sulfidation epithermal deposits. In: Thompson, J.F.H. (Ed.), Magmas, Fluids and Ore Deposits. Mineralogical Association of Canada Short Course Series, vol. 23, pp. 455–477.

Simmons, S.F., Gemmell, J.B, Sawkins, F.J., 1988. The Santo Niño silver–lead–zinc vein, Fresnillo District, Zacatecas, Mexico: Part II. Physical and chemical nature of ore-forming solutions. Economic Geology 83, 1619–1641.

Taylor Jr., H.P., 1974. The application of oxygen and hydrogen isotope studies to the problem of hydrothermal alteration and ore deposition. Economic Geology 69, 843–883.

Taylor, B.E., 1992. Degassing of H_2O from rhyolite magma during eruption and shallow intrusion, and the isotopic composition of magmatic water in hydrothermal systems. In: Hedenquist, J.W. (Ed.), Extended Abstracts, Japan–U.S. Symposium on Magmatic Contributions to Hydrothermal Systems. Reports of the Geological Survey of Japan, vol. 279, pp. 190–194.

Tolstikhin, I.N., Mamyrin, B.A., Khabarin, L.V., Erlikh, E.N., 1974. Isotope composition of helium in ultrabasic xenoliths from volcanic rocks of Kamchatka. Earth and Planetary Science Letters 22, 75–84.

Torgersen, T., Lupton, J.E., Sheppard, D.S., Giggenbach, W.F., 1982. Helium isotope variations in the thermal areas of New Zealand. Journal of Volcanology and Geothermal Research 12, 283–298.